Four-point Bending Testing of 8-in. (200-mm) Diameter TR-XTREME™ Ductile Iron pipe

Shih-Hung Chiu

Qinglai Zhang

Shakhzod Takhirov

Kenichi Soga

I

EXECUTIVE SUMMARY

This report describes the experimental and numerical results of four-point bending tests performed on an 8-inch TR-XTREME^{TM} earthquake-resistant ductile iron pipe manufactured by U.S. Pipe. The tests aim to characterize the relationship between rotation and moment of the restrained joint and the magnitude of joint rotation that initiates significant joint damage or water leakage. Two four-point bending tests were performed for two different orientations of the locking segments at the bell joint connection. In addition, the experimental results obtained from distributed fiber optic strain sensors were used to validate the three-dimensional (3D) finite element (FE) models, which can be used as the reference model for optimizing the pipeline design, installation, and risk assessment.

Keywords: *Ductile iron pipe, jointed water pipelines, four-point bending, fiber optic sensing, finite element analysis.*

ACKNOWLEDGMENTS

DISCLAIMER

Any opinions, findings, conclusions, or recommendations expressed in this report are those of the author(s) and do not necessarily reflect those of the University of California, Berkeley.

CONTENTS

LIST OF FIGURES

LIST OF TABLES

1. Introduction

This report presents the experimental and finite element modeling results of the four-point bending tests performed on 8-inch TR-XTREME™ earthquake-resistant ductile iron pipe specimens manufactured by U.S. Pipe. The pipe is designed to maintain full water service after seismic events to achieve the seismic resiliency of the pipeline systems. The pipe has a single-restrained bell joint connection, providing 2.9-inch horizontal movement and 5-degree deflection contraction capacity. The schematic of the bell joint is shown in Figure 1-1. The spigot is designed to be inserted into the bell, passing through a water-prevent rubber gasket, and is equipped with a weld bead to bear against the locking segments, used as a locking mechanism while pulling. The single slot is used for holding the locking segments. Three white stripes on the spigot are used to indicate the installation position. The manufacturer recommends three installation positions: collapsed, midpoint, and extended location, as shown in Figure 1-2. In this study, the experiment started from the fully extended position (i.e., Option C), meaning that the weld bead on the spigot contacted the locking segments at the initial stage.
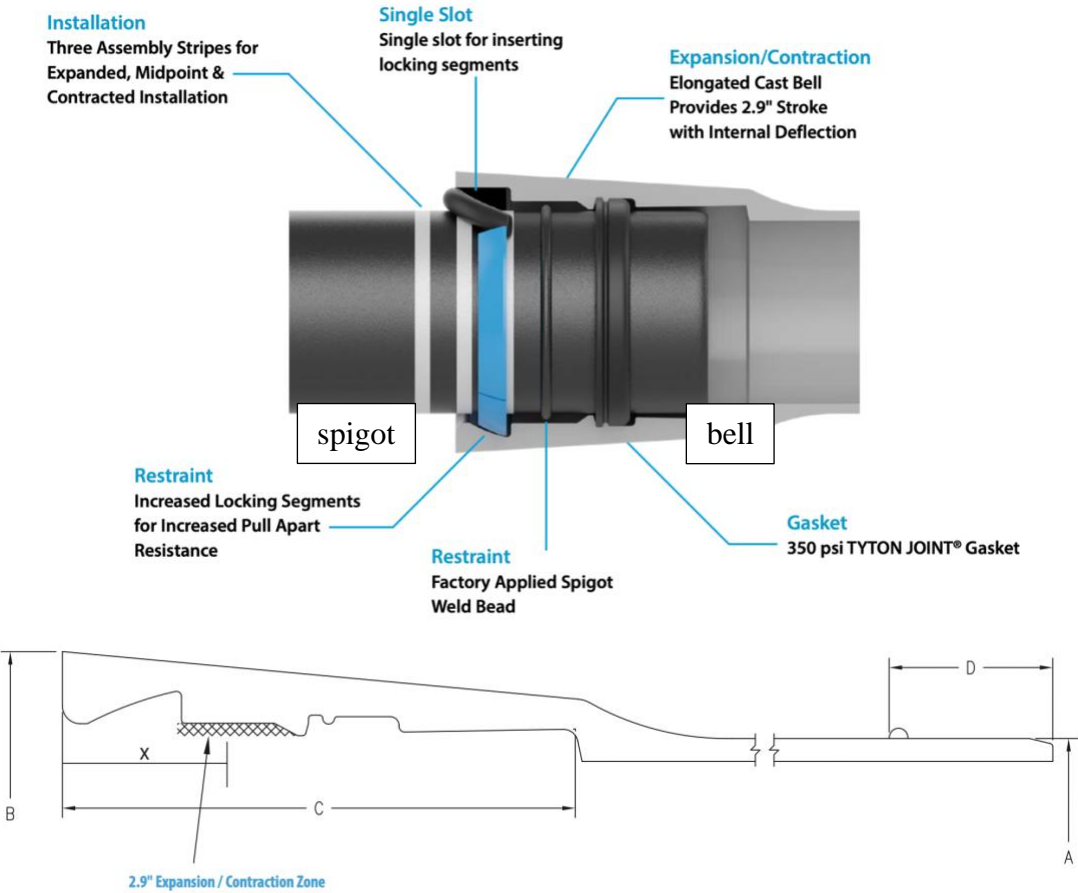
Figure 1-1 Mechanism of TR-XTREME™ joint (U.S. Pipe, 2020)

Option A-Collapsed – Correct assembly is determined when the front edge of the assembly stripe furthest from the spigot tip lines up with the face of the pipe bell as viewed from above, leaving only one assembly stripe shown.
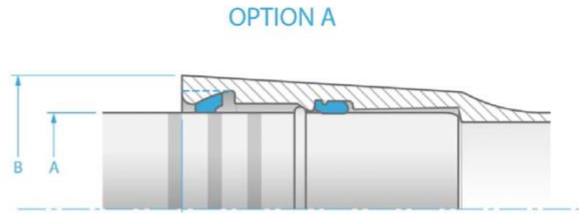
Option B-Midpoint – Correct assembly is determined when the front edge of the middle assembly stripe lines up with the face of the pipe bell as viewed from above, leaving two assembly stripes shown.
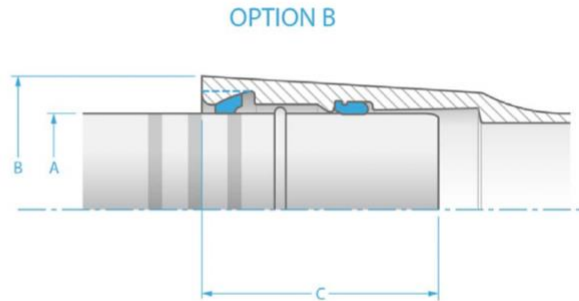
Option C-Extended (Restrained) - Correct assembly is determined when the front edge of the assembly stripe closest to the spigot tip lines up with the face of the pipe bell as viewed from above, leaving three assembly stripes shown. This is the proper assembly when immediate joint restraint is required.
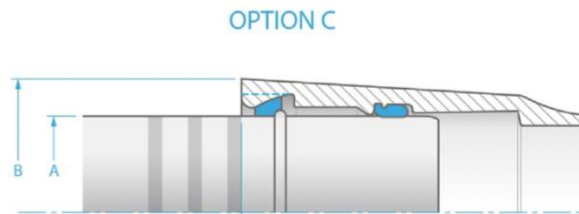
Figure 1-2 Recommended installation positions (U.S. Pipe, 2020)

Two 8-inch TR-XTREME™ pipes with two different orientations of locking segments (the single slot located at 9 o'clock and 12 o'clock, respectively) were used for the four-point bending tests. A vertical force was applied to the pipelines, forcing the joint to rotate until severe pipe damage or water leakage occurred. The testing objectives are (1) to characterize the joint response to rotation beyond the deflection limit and (2) to discuss the effect of the different locking segment orientations on the pipe performance under four-point bending conditions.

In this study, distributed fiber optic sensors (DFOS) were utilized to measure the continuous strain development of the pipeline in the longitudinal and circumferential directions. In addition, a finite element (FE) analysis was conducted to simulate the behavior of the pipelines by utilizing an elastoplastic material model in ABAQUS. The data from DFOS were then used to validate the predicted results from the FE model. The validated FE model can be used for future parametric studies.

2. Test Setup

2.1 Experimental Setup

The experimental setup was developed at the Center for Smart Infrastructure (CSI) of UC Berkeley. The design of the experimental setup is shown in Figure 2-1. An actuator was located above the center line, defined as 3.25 inches away from the bell face. A steel spreader beam was located beneath the actuator used to transfer the force to the loading saddles, placed about 33.5 inches from the center line on the spigot and the bell pipe. Both pipes were supported on the rollers located 100.5 inches from the center. The overview of the fully assembled setup of the four-point bending test is shown in Figure 2-2.
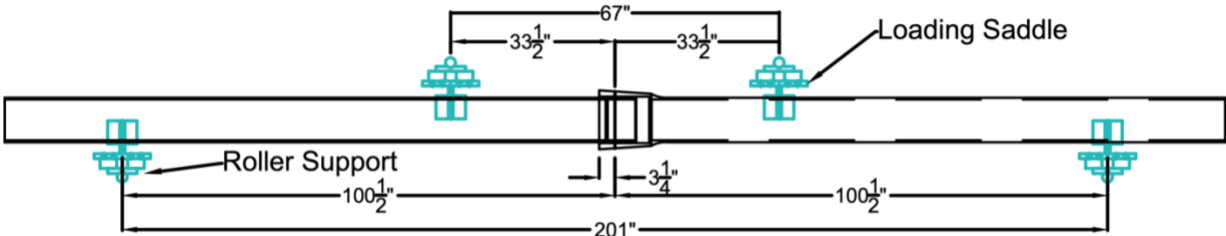
Figure 2-1 Experimental setup design

Figure 2-2 Overview of the experimental setup

The 8-inch TR-XTREME^{TM} pipes, made of ductile iron, were manufactured by U.S. Pipe. As described earlier, the manufacturer recommends three assembly locations, collapsed, midpoint, and extended. For the experiments, the extended location (i.e., three white stripes on the spigot are visible) was used as the initial location, meaning that the locking segments were initially in contact with the weld bead on the spigot.

The testing procedure includes three stages: water pressurization, self-weight moving down, and actuator pushing down. Firstly, the pipes were pressurized to 50 psi. Then the temporary supports were removed to allow the pipes to move down due to their self-weight, which introduced rotations to the specimen. Finally, the actuator pushed the pipeline further down to reach a larger rotation until severe pipe damage and water leakage were observed.

2.2 Specimen List

Two four-point bending tests were conducted with the same experimental setup but different orientations of the locking segments. For the first test, the single slot was rotated in the 12 o'clock direction (i.e., at the top side), where the three pieces of the locking segments were placed at the west, east, and bottom sides (3, 6, 9 o'clock). For the second test, the single slot was located in the 9 o'clock direction (i.e., at the west side), where the three pieces of the locking segments were placed at the top, east, and bottom sides (3, 6, 12 o'clock), respectively, as shown in Figure 2-3. The test log is presented in Table 2-1.

12 o'clock orientation (Specimen 1)   **9 o'clock orientation (Specimen 2)**
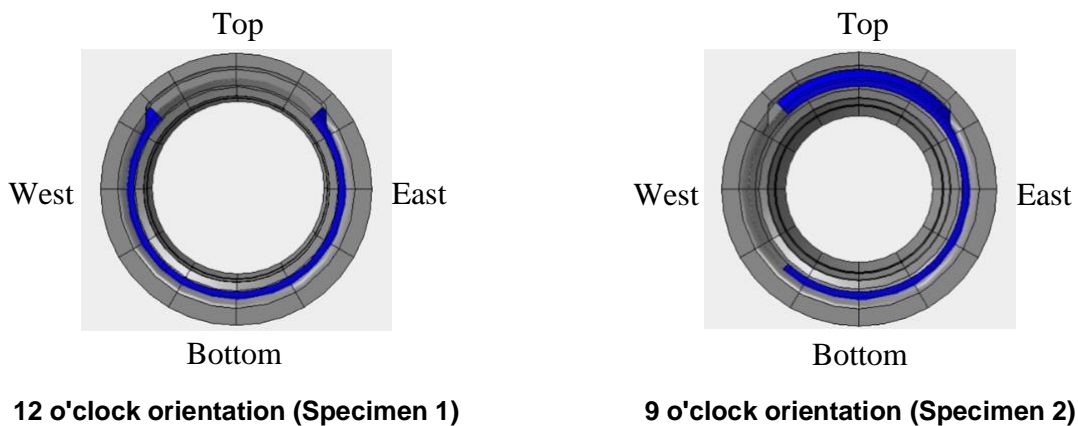
Figure 2-3 Locking segments orientation

Table 2-1 Test log

Test No	Specimen	Test date	Locking segments orientation
1	Specimen 1	11/30/2022	12 o'clock
2	Specimen 2	12/15/2022	9 o'clock

3.Instrumentation

The instrumentation consisted of conventional instruments (strain gauges, string pots) and distributed fiber optic sensors (DFOS).

3.1   Conventional Instruments

The locations of the instruments are shown in Figure 3-1, and the local instrumentation names are shown in Table 3-1.

Strain gauges were installed at four planes; two on the bell pipe and another two on the spigot. Each plane consisted of four strain gauge sets. Each set of strain gauges included two strain gauges in the perpendicular directions measuring axial and circumferential strains. A total of 32 strain gauges were installed. Strain gauge sets were placed at about 20 degrees apart from the quarter points due to the installation conflict with distributed fiber optic sensors.

Four wire pots were placed on the bell pipe at 45 degrees apart from the quarter points around the circumference and were fixed to the spigot to measure the joint opening. Another four wire pots were used to measure the pipe displacement during the experiment. They were mounted to the bell pipe and spigot on the east and bottom sides individually. The wire pots installed on the bottom sides were used to monitor the vertical displacement, and the ones on the east side aimed to measure the horizontal movement. A total of eight wire pots were installed.
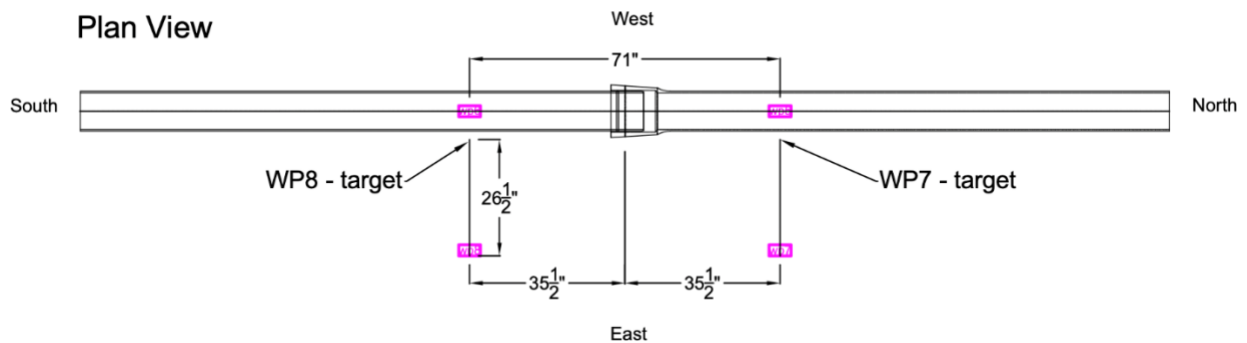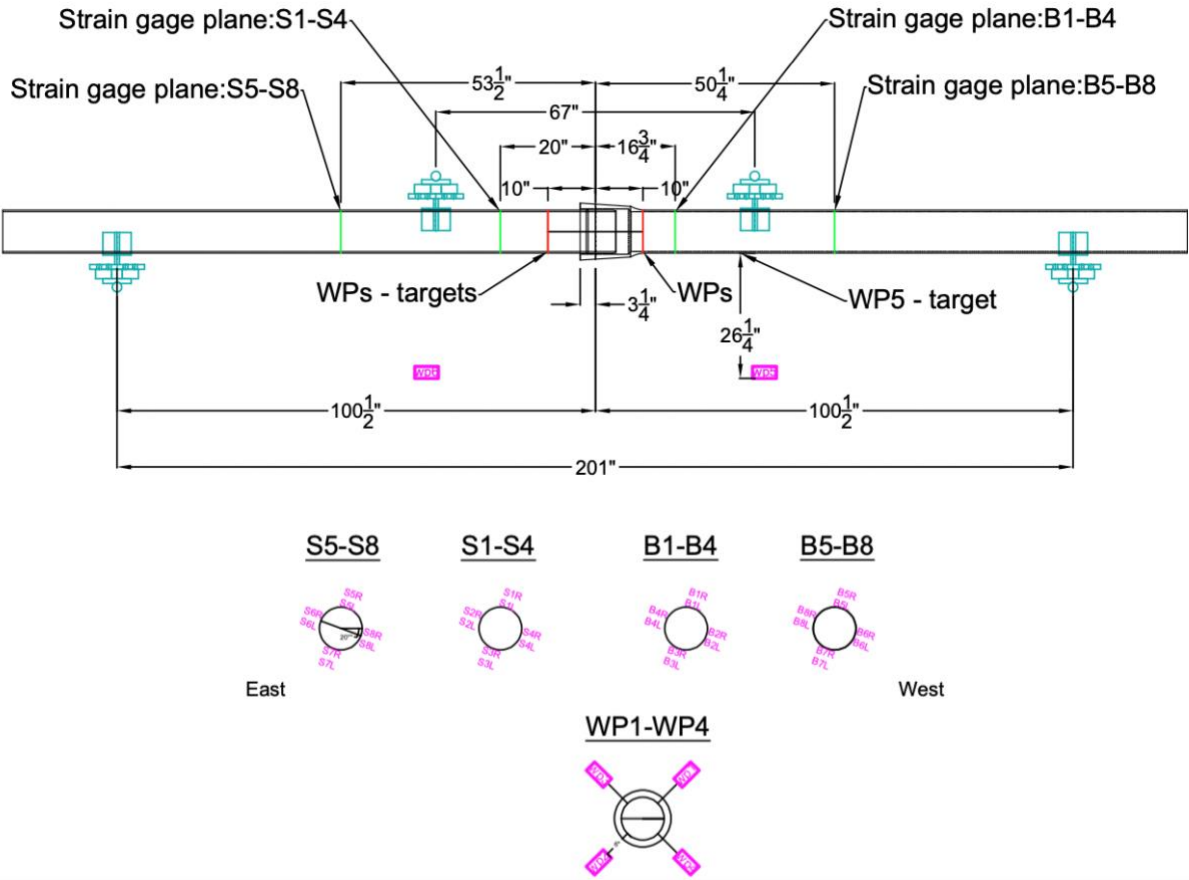
Figure 3-1 Instrumentation plan of conventional instruments

Table 3-1 Conventional instrumentation local names

Instrument	Location	Local Instrument Name
String Pot	Parallel to Axial Direction, North of Bell, Top-west	wp1
	Parallel to Axial Direction, North of Bell, West-bottom	wp4
	Parallel to Axial Direction, North of Bell, Bottom-east	wp2
	Parallel to Axial Direction, North of Bell, East-top	wp3
	Perpendicular to Axial Direction, North of Bell, Bottom	wp5
	Perpendicular to Axial Direction, North of Bell, East	wp7
	Perpendicular to Axial Direction, South of Bell, Bottom	wp6
	Perpendicular to Axial Direction, South of Bell, East	wp8
Strain Gauge	Top of Bell-side Pipe (North), Axial Strain	B5L
	West of Bell-side Pipe (North), Axial Strain	B6L
	Bottom of Bell-side Pipe (North), Axial Strain	B7L
	East of Bell-side Pipe (North), Axial Strain	B8L
	Top of Spigot (North), Axial Strain	S1L

14

East of Spigot (North), Axial Strain	S2L
Bottom of Spigot (North), Axial Strain	S3L
West of Spigot (North), Axial Strain	S4L
Top of Bell-side Pipe (North), Circumferential Strain	B5R
West of Bell-side Pipe (North), Circumferential Strain	B6R
Bottom of Bell-side Pipe (North), Circumferential Strain	B7R
East of Bell-side Pipe (North), Circumferential Strain	B8R
Top of Spigot (North), Circumferential Strain	S1R
East of Spigot (North), Circumferential Strain	S2R
Bottom of Spigot (North), Circumferential Strain	S3R
West of Spigot (North), Circumferential Strain	S4R
Top of Bell-side Pipe (South), Axial Strain	B1L
West of Bell-side Pipe (South), Axial Strain	B2L
Bottom of Bell-side Pipe (South), Axial Strain	B3L
East of Bell-side Pipe (South), Axial Strain	B4L
Top of Spigot (South), Axial Strain	S5L
East of Spigot (South), Axial Strain	S6L
Bottom of Spigot (South), Axial Strain	S7L
West of Spigot (South), Axial Strain	S8L
Top of Bell-side Pipe (South), Circumferential Strain	B1R
West of Bell-side Pipe (South), Circumferential Strain	B2R
Bottom of Bell-side Pipe (South), Circumferential Strain	B3R
East of Bell-side Pipe (South), Circumferential Strain	B4R
Top of Spigot (South), Circumferential Strain	S5R
East of Spigot (South), Circumferential Strain	S6R
Bottom of Spigot (South), Circumferential Strain	S7R
West of Spigot (South), Circumferential Strain	S8R

3.2 Distributed Fiber Optic Sensors

Two types of fiber optic cables manufactured by NanZee Sensing Technology Co. were used; (a) 5 mm diameter armored cable (NanZee 5mm) and (b) 0.9 mm diameter cable (NanZee 0.9mm). The local instrument names are listed in Table 3-2, and the layouts of the cables are shown in Figure 3-2. 3M SCOTCH-WELD DP8010 epoxy was used to attach the cables to the pipes.

NanZee 5mm cables (blue lines), which are commonly used in the field due to their robustness, were used in the longitudinal direction to check their performance for actual field application. They were attached on both pipes, 90 degrees apart, numbered F12-F19. To better understand the deformation mechanism of the pipes and bell section, NanZee 0.9mm cables (red lines), which are fragile but cost-effective in laboratory conditions, were used for measuring circumferential strains, numbered F1-F11. Four circumferential sensors with about 18-inch spacing were installed on both pipes. In addition, another three circumferential sensors were

attached to the bell end, the middle of the section, and the location on top of the locking segments (i.e., about 3.5 inches from the bell face).

A Rayleigh-based optical frequency domain reflectometry (OFDR), Luna ODiSI 6100 series, was used in this experiment for data acquisition. The analyzer is capable of measuring up to 50m long fiber optic cable with an accuracy of less than ±1 micro strain when taking a measurement every 0.65mm. Further details about the cables and analyzer can be found in Appendix A.
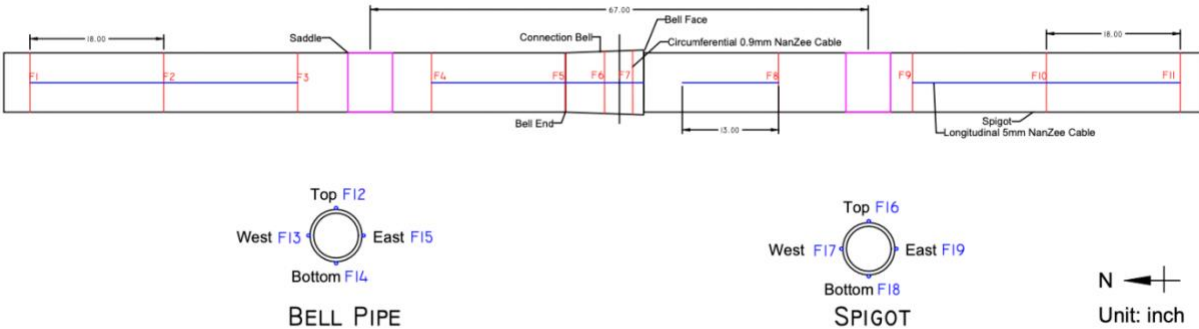
Figure 3-2 DFOS instrumentation plan

Table 3-2 DFOS local names

Instrument	Location	Local Instrument Name
DFOS	82.5 inches north of bell face, Circumferential	F1
	64.5 inches north of bell face, Circumferential	F2
	46.5 inches north of bell face, Circumferential	F3
	28.5 inches north of bell face, Circumferential	F4
	Bell end, Circumferential	F5
	Mid location of bell, Circumferential	F6
	3.5 inches north of bell face Circumferential	F7
	18 inches south of bell face, Circumferential	F8
	36 inches south of bell face, Circumferential	F9
	54 inches south of bell face, Circumferential	F10
	72 inches south of bell face, Circumferential	F11
	Bell pipe, Top, Longitudinal	F12
	Bell pipe, West, Longitudinal	F13
	Bell pipe, Bottom, Longitudinal	F14
	Bell pipe, East, Longitudinal	F15
	Spigot, Top, Longitudinal	F16
	Spigot, West, Longitudinal	F17
	Spigot, Bottom, Longitudinal	F18
	Spigot, East, Longitudinal	F19

4. Test Results

All test results are discussed in this section. In addition, a summary of the failure mode and performance of the 8 inches TR-XTREME™ ductile iron pipe is included.

4.1 Calculation Approach

The approaches to calculating the rotation and moment are discussed herein. The pipes are assumed to be rigid bodies, and the rotations of the pipes are computed using equations (1) – (3). The vertical displacements of the pipes were measured by the vertical wire pots (VWP) located beneath the pipes. θ_{bell} and θ_{spigot} are the rotations of the west pipe and the east pipe, respectively. The overall rotation, θ_{Total}, of the joint is defined as the sum of the two side angles.

$$\theta_{bell} = \tan^{-1}(\frac{vertical\ displacement\ of\ bell\ pipe}{distance\ between\ VWP\ and\ the\ end\ support}) \tag{1}$$

$$\theta_{spigot} = \tan^{-1}\left(\frac{vertical\ displacement\ of\ spigot}{distance\ between\ VWP\ and\ the\ end\ support}\right) \tag{2}$$

$$\theta_{Total} = \theta_{bell} + \theta_{spigot} \tag{3}$$

The system is considered to be a simple-supported beam. The self-weight, including the weight of the pipe and water, is assumed to be evenly distributed, and hence the moment ($M_{distrib}$) introduced by self-weight is calculated based on equation (4), where w is the uniform load due to the self-weight, and l is the length of the pipe between the outer supports. The uniform weight (w) is 4.5 lbs/in and the distance between the supports (l) is 201 inches. The additional moment ($M_{central}$) applied to the central portion of the pipe is calculated using equation (5), where P is the actuator load, and L is the distance between the support and the loading location. The distance between the loading point and the support is 67 inches.

$$M_{distrib} = \frac{wl^2}{8} \tag{4}$$

$$M_{central} = \frac{PL}{2} \tag{5}$$

4.2 Experimental Data Analysis

4.2.1 Moment and Rotation

The pipes were filled with water and pressurized to 50 psi. Then, the supporting jacks located beneath the loading saddle were removed to allow the pipes to move downward. After the pipes reached the static force equilibrium status, a monotonic force perpendicular to the longitudinal axis of the pipeline was applied at the center point of the load transfer beam. Then,

the force was transferred to the pipes via the two loading saddles. The moments and rotations of each specimen were calculated using the formulas mentioned above, and the results are shown in Figure 4-1. Due to the location conflict between the experimental setup and the vertical wire pots, the self-weight moving down stage results were not recorded. Figure 4-1 shows only the measured moment and rotation relationships during the actuator pushing down stage. The result of self-weight moving down stage will be discussed in Chapter 5 using the finite element model simulation. The maximum rotations with corresponding moments of each specimen are 1) 13.2 degrees rotation with 763.6 kip-in moments, and 2) 13.1 degrees rotation with 1153.2 kip-in moments. Although the maximum moments vary, the ultimate rotations are similar for both specimens. Water leakage was found around the 14-degree joint rotation for both specimens.
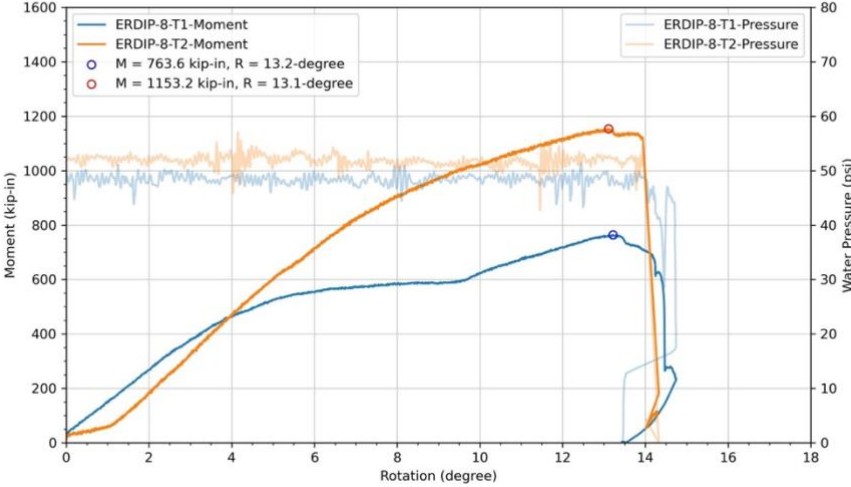

Figure 4-1 Moment, rotation, and water pressure of the tests

The difference in the moment response is due to the orientation difference of the locking segments. Specimen 1 constantly requires a smaller moment to achieve the desired rotation after reaching a 4-degree rotation. Instead of having a locking segment at the top side (12 o'clock) location, Specimen 1 has a rubber gasket to seal the single slot, which allows a small moment resistance. Therefore, Specimen 1 tends to have a smaller moment resistance with a similar applied displacement than Specimen 2.

However, the curves at the early test stage of less than 4 degrees of rotation show that Specimen 1 required a larger moment for a given rotation. It is hypothesized that the initial experimental setup imperfection may be the reason for the observed difference. Ideally, the spigot inside the bell section would sit on the bedding, as shown in Figure 4-2. But it is possible that the spigot of Specimen 2 was sitting on the edge of the bedding and fell into the groove at the early stage of the Specimen 2 test. Therefore, before the spigot fully bears against the bell, it was suspected that Specimen 2 required a smaller moment than Specimen 1 to achieve the desired rotation.
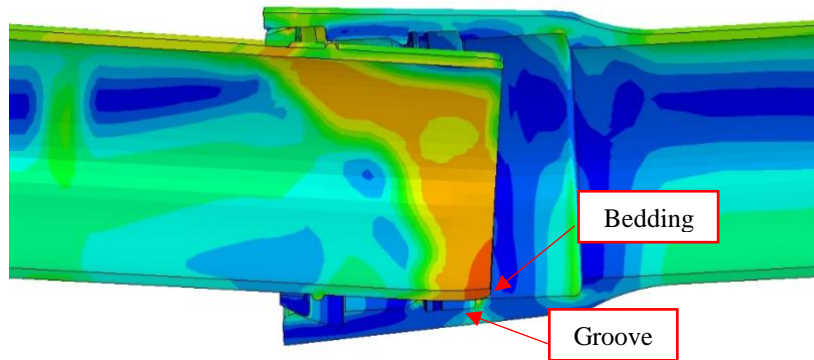
Figure 4-2 Sketch of the internal joint

Both tests failed when the specimens reached around 13 degrees of rotation during the actuator push down stage, regardless of the locking segment placement, meaning that the failure is not governed by the overall moment force but by more localized ones. Significant water leakage can be observed after the pipe fails, around a 14 degrees of rotation.

4.2.2 Failure Modes

The experiments were designed to test up to a pipe failure or a significant water leakage resulting in a large water pressure drop. The tests were stopped due to the failure at the bottom side of the spigot. The pipe failed with severe water leakage when the moment reached 763.6 and 1153.2 kip-in for Specimen 1 and 2, respectively. This means that the orientation of the locking segments would be influential to the moment required to reach a given rotation. However, a similar rotation capacity was found. Both pipes reached about 13 degrees of rotation during the actuator pushing down stage before a significant water pressure drop. This indicates that different locking segment orientation does not seem to influence the rotation capacity of the joint.

Figure 4-3 shows the Mises stress obtained from the finite element (FE) models for both specimens at 11 degrees of rotation during the actuator pushing down stage. The detail of the FE models will be discussed in the next chapter. The FE analysis results show that the Mises stress values at the bottom of the spigot (indicated by the orange and red range) exceed the yield stress of 42,000 psi in both specimens. This observation suggests that the bottom of the spigots experience plastic strains under bending, resulting in permanent deformation and an increased risk of failure. The failure patterns were the same in both specimens. The upper section of the joint remained in an elastic state for both specimens. This finding implies that the orientations of the locking segments have minimal influence on the joint rotation capacity.
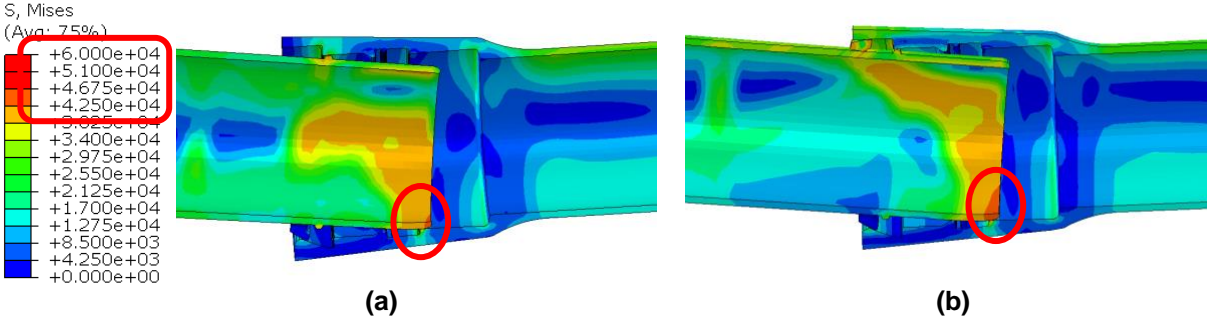
Figure 4-3 Mises stress distribution of the specimens at 11 degrees of rotation. (a) Specimen 1, (b) Specimen 2

Figure 4-4 shows the failure pattern of Specimen 1. The primary failure occurred in the spigot, as shown in Figure 4-4 (b). The spigot was distorted at the section where it was inserted into the pipe. Moreover, since the bottom side of the spigot was bearing against the bell invert, a failure was found on the bottom side of the spigot, which resulted in water leakage.
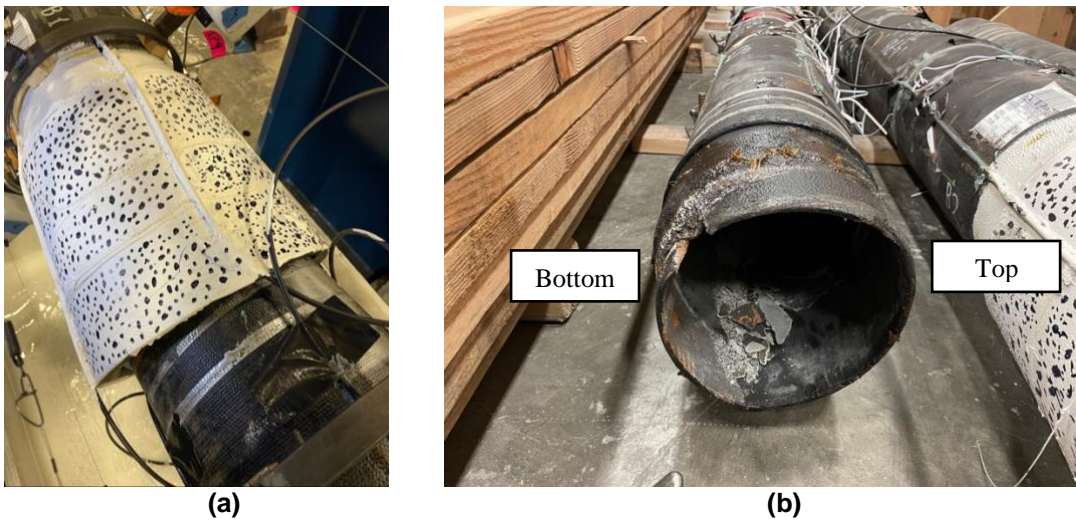

Figure 4-4 Failure of Specimen 1. (a) Bell, (b) Spigot

The failure pattern of Specimen 2 is shown in Figure 4-5. No crack was found on the bell. The primary failure occurred in the spigot. At the bottom of the spigot, a breakage similar to that of Specimen 1 can be found. Moreover, a 45-degree crack propagated from the west through the bottom to the east was observed. The crack was caused by shear force. When the bottom side of the spigot was bearing against the invert of the bell and the top of the spigot was contacting the bell crown, a shear force was introduced, as shown in Figure 4-6.

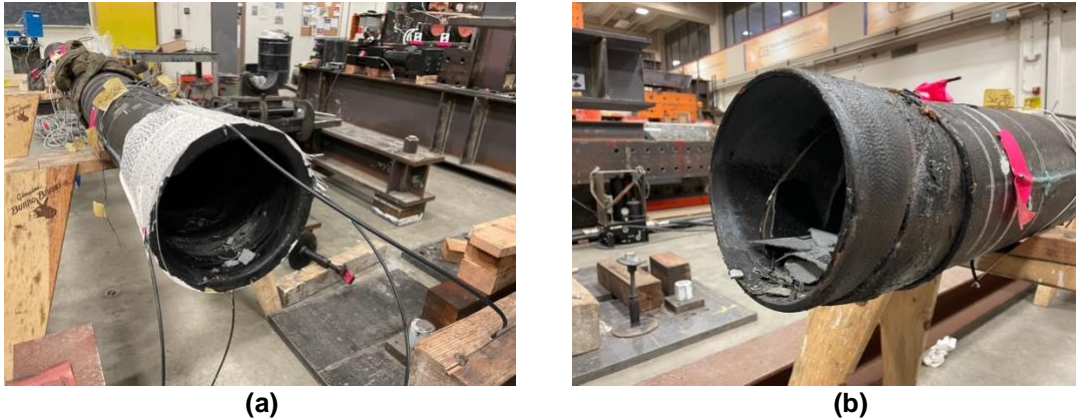The summary of the test results is listed in Table 4-1.

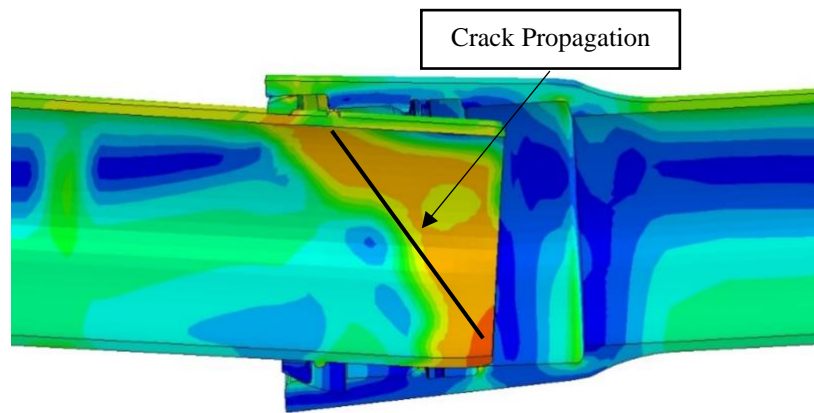**Figure 4-5 Failure of Specimen 2. (a) Bell, (b) Spigot**

Crack Propagation

Figure 4-6 Sketch of the failure mechanism

Table 4-1 Summary of the tests

	Locking Segments Orientation	Max. Moment (kip-in)	Max. Rotation (degree)
Specimen 1	12 o'clock	763.6	13.2
Specimen 2	9 o'clock	1153.2	13.1

4.2.3 Axial Strains

The axial strain results measured by the strain gauges attached to Specimen 1 and 2 are shown in Figure 4-7 and Figure 4-8, respectively. For both specimens, a clear pattern can be observed; that is, the top side (12 o'clock) is generally under compression due to the bending, whereas the bottom side (6 o'clock) is mainly under tension. Theoretically, the axial strains at the east side (3 o'clock) and west side (9 o'clock) would be close to zero. However, the strain gauges were attached 20-degree offset from the quarter points due to the installation conflict. The strain gauges labeled "west" were placed 20 degrees toward the bottom side (6 o'clock), and

the ones labeled "east" were located 20-degree toward the top side (12 o'clock), resulting in compression on "east" and tension on "west."

For Specimen 1, the strain distribution patterns on both sides of the pipe were similar. However, Specimen 2 showed different strain distributions at the locations closer to the bell (i.e., bell pipe-south, spigot-north). As discussed in the previous section, the spigot might not bear against the designed bedding inside the bell; instead, the spigot might fall into the groove. Figure 4-2 shows the ideal case of the bell under a bending force, meaning that the spigot is sitting on the bedding where the wall is thicker. However, during the test, since the bedding is short and the spigot is likely to fall into the groove, the spigot might be bearing against the groove where the wall is thinner, contributing to a more significant strain around the bell. As a result, the strain gauges located near the bell gave a larger magnitude of the strains than those placed further away. In addition, Specimen 2 has a non-symmetric configuration of the locking segments (i.e., locking segments were placed on the east side but not on the west side). Since the locking segment provides a better constraint than the rubber gasket, the pipe tends to move more on the rubber gasket side, resulting in an out-of-plane rotation. The continuous DFOS data can clearly observe the phenomenon, which is discussed in the following section.
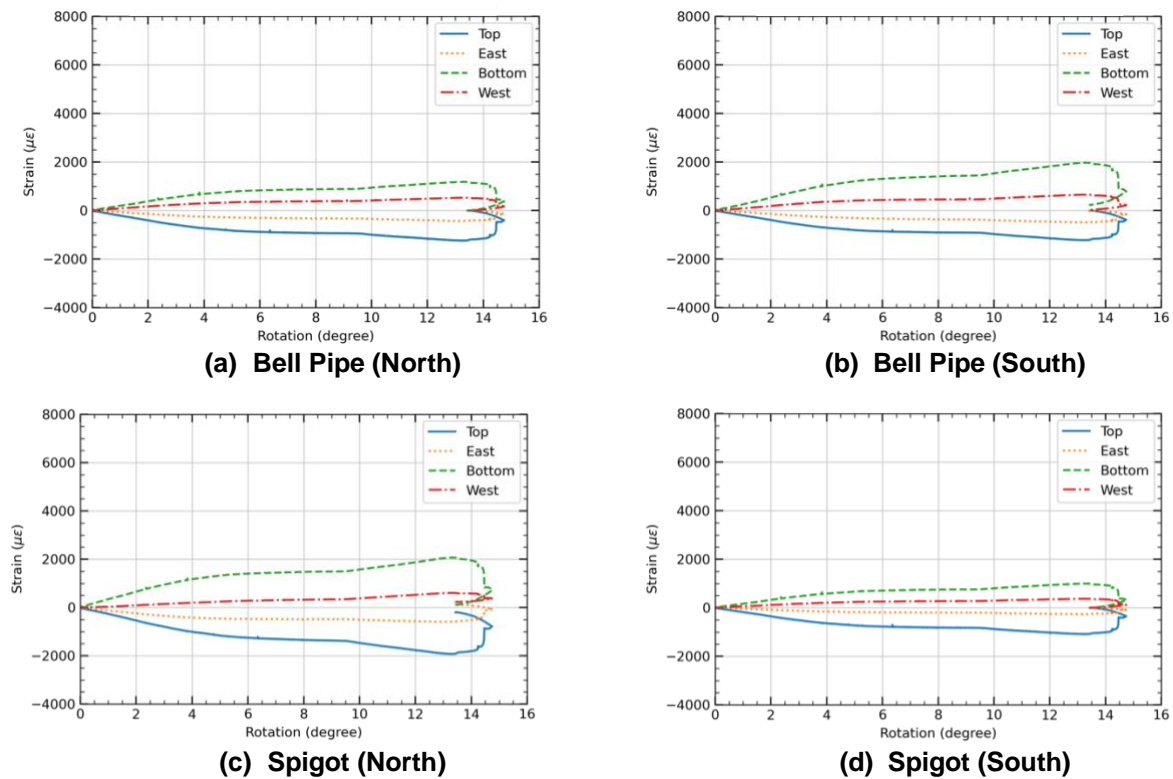

(a) Bell Pipe (North)

(b) Bell Pipe (South)

(c) Spigot (North)

(d) Spigot (South)

Figure 4-7 Axial strain vs. rotation of Specimen 1

22

(a) Bell Pipe (North)   **(b) Bell Pipe (South)**

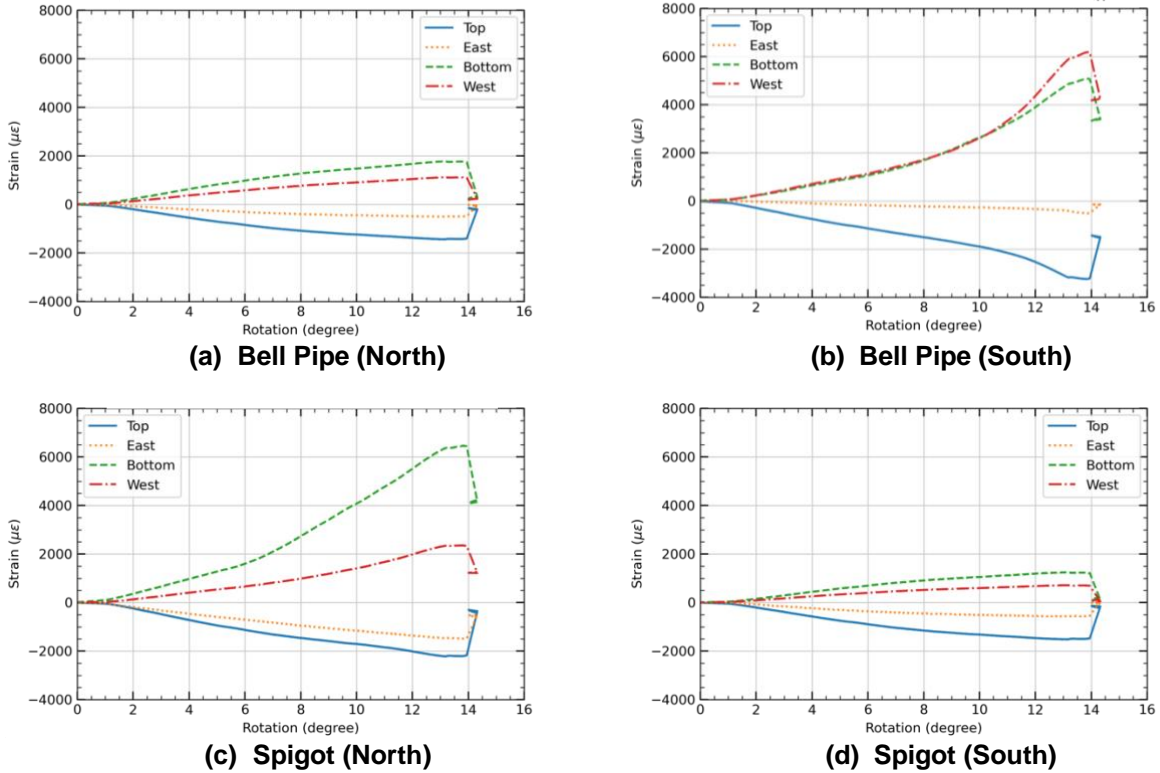**(c) Spigot (North)**   **(d) Spigot (South)**

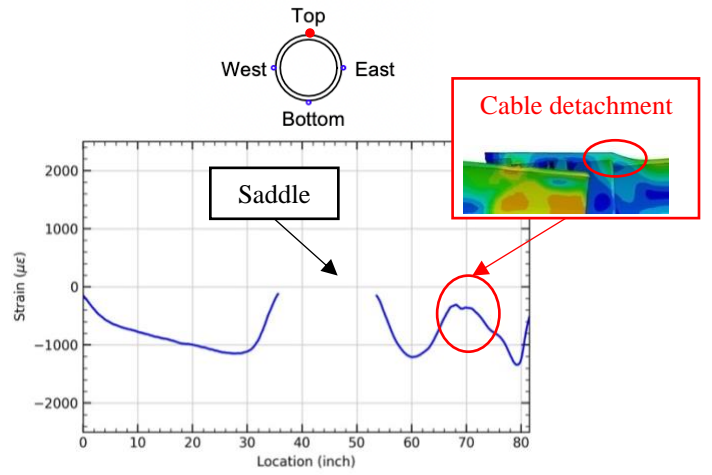**Figure 4-8 Axial strain vs. rotation of Specimen 2**

The axial strain results of Specimen 1 measured by DFOS are shown in Figure 4-9 and Figure 4-10. All the strain distributions of the sensors are plotted from the north to the south. The plots showed the strain distribution when the total rotation reached about 12.5 degrees. Similar to the observation made in the strain gauge data, the top side (12 o'clock) was experiencing compression, whereas the bottom side (6 o'clock) was experiencing tension.

An anomalous strain distribution can be observed at the top side of the bell pipe close to the bell section, as shown in Figure 4-9(b). The reason for this is cable detachment. The detached location is close to the edge between the bell and the pipe where a slope exists. Because of the slope, the fiber optic cable was not fully attached to the pipe.

The strains at the sides of the pipe (i.e., 3 and 9 o'clock) were generally minimal. However, compressive strain can be found at the location on the west side (9 o'clock) of the bell pipe, as shown in Figure 4-9(c). For the spigot, compressive strains are recorded on the east side (3 o'clock) and tensile strains on the west side (9 o'clock), both at locations close to the bell. These results indicate an out-of-plane rotation happened inside the bell between the spigot and the bell pipe.
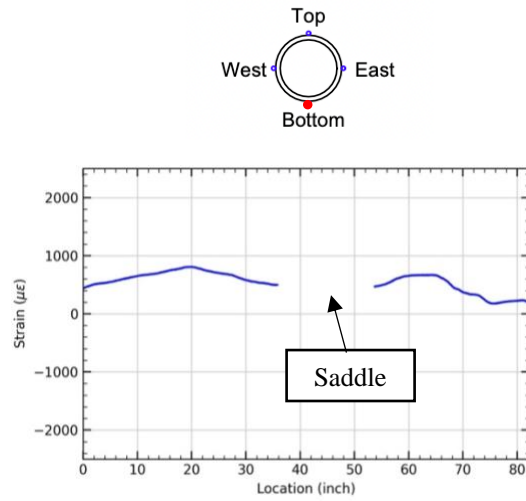
23
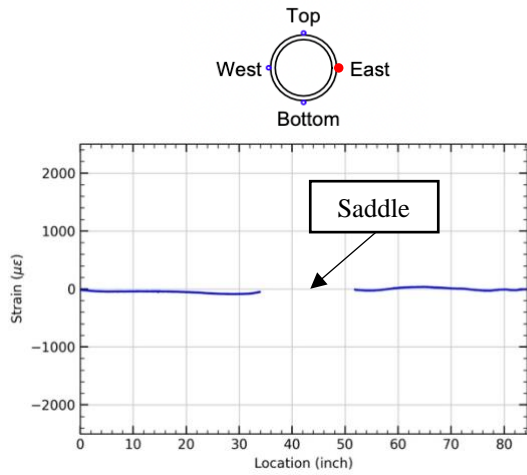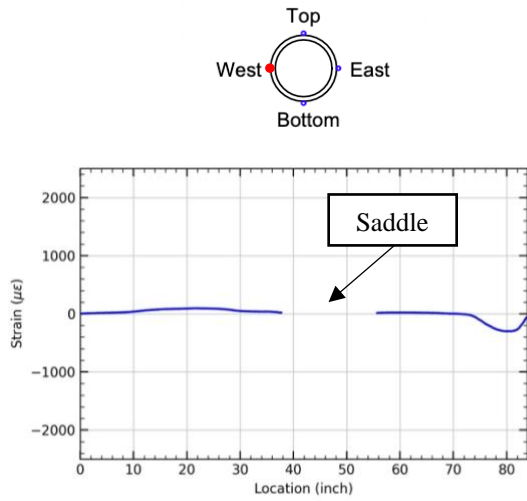
Figure 4-9 Axial strain development of bell pipe of Specimen 1 under 12.5-degree rotation condition. (a) East side, (b) Top side, (c) West side, (d) Bottom side
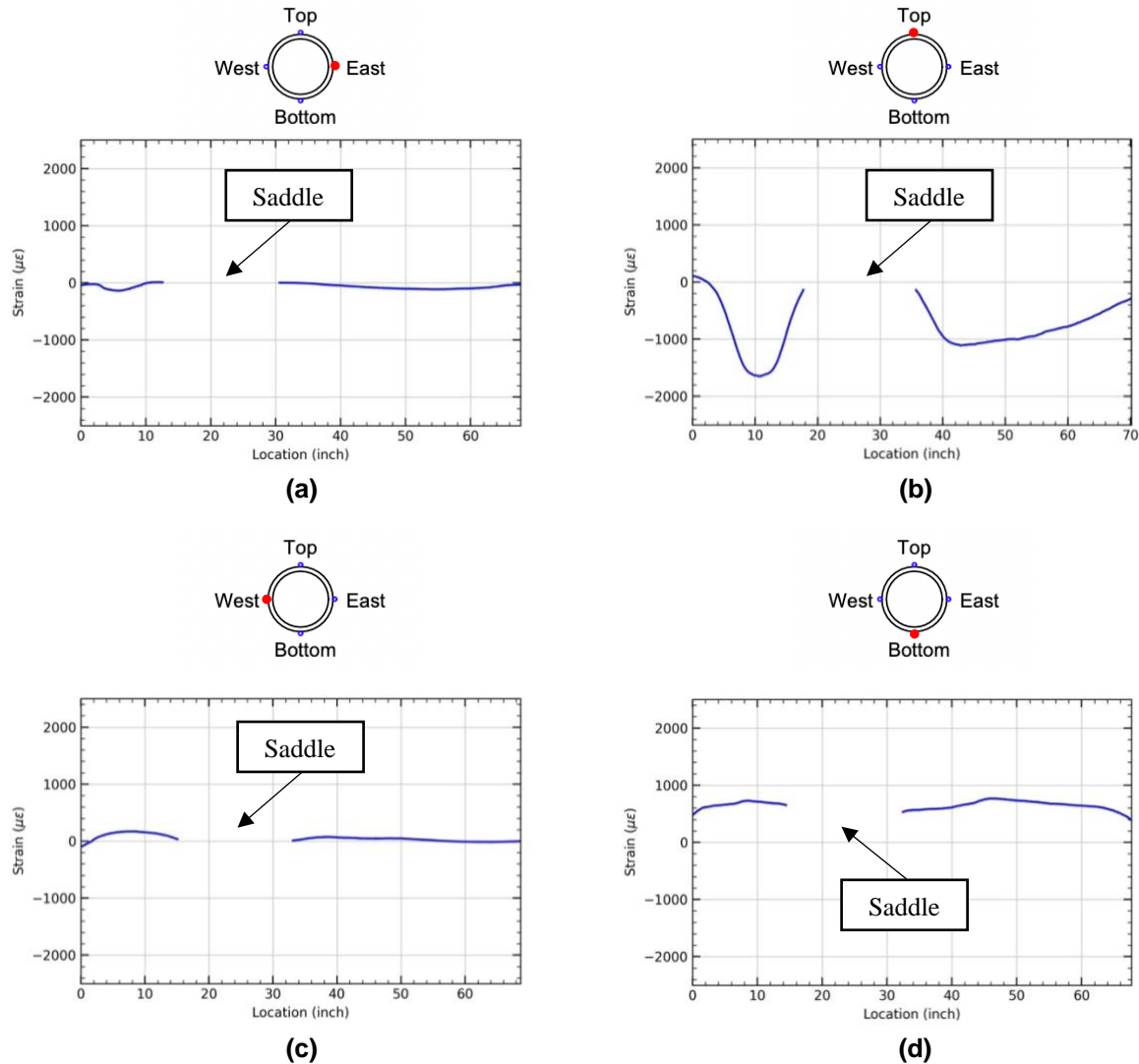
Figure 4-10 Axial strain development of spigot of Specimen 1 under 12.5-degree rotation condition. (a) East side, (b) Top side, (c) West side, (d) Bottom side

Figure 4-11 and Figure 4-12 show the axial strain distributions of the bell pipe and spigot, respectively, in Specimen 2. The general trend of the strain distributions is similar to that of Specimen 1; that is, tensile strains on the bottom side (6 o'clock), compressive strains on the top side (12 o'clock), and minor strains on the remaining two sides (3 and 9 o'clock). However, the magnitude of the strains is generally more significant than those measured in Specimen 1, especially at locations close to the bell section. The reason might again be that the spigot inside the bell was sitting on the groove instead of the bedding that was designed to sit on. Since the wall is thinner at the groove than at the bedding, a larger magnitude of strains was measured at the locations close to the bell.

An out-of-plane rotation at the bell section can be found in Specimen 2. Looking at the strain distributions on the east and west sides (3 and 9 o'clock) close to the bell section, one can observe that the magnitudes of the strain at these locations are larger than those further away from the bell. This is due to the non-symmetric locking segment placement described in the

25

previous section. Tensile strains were observed on the east side (3 o'clock) close to the bell on both pipes. Compressive strains were shown on the spigot's west side (9 o'clock). This indicates that an out-of-plane rotation happened and was bending toward the west (9 o'clock), where the rubber gasket was placed.
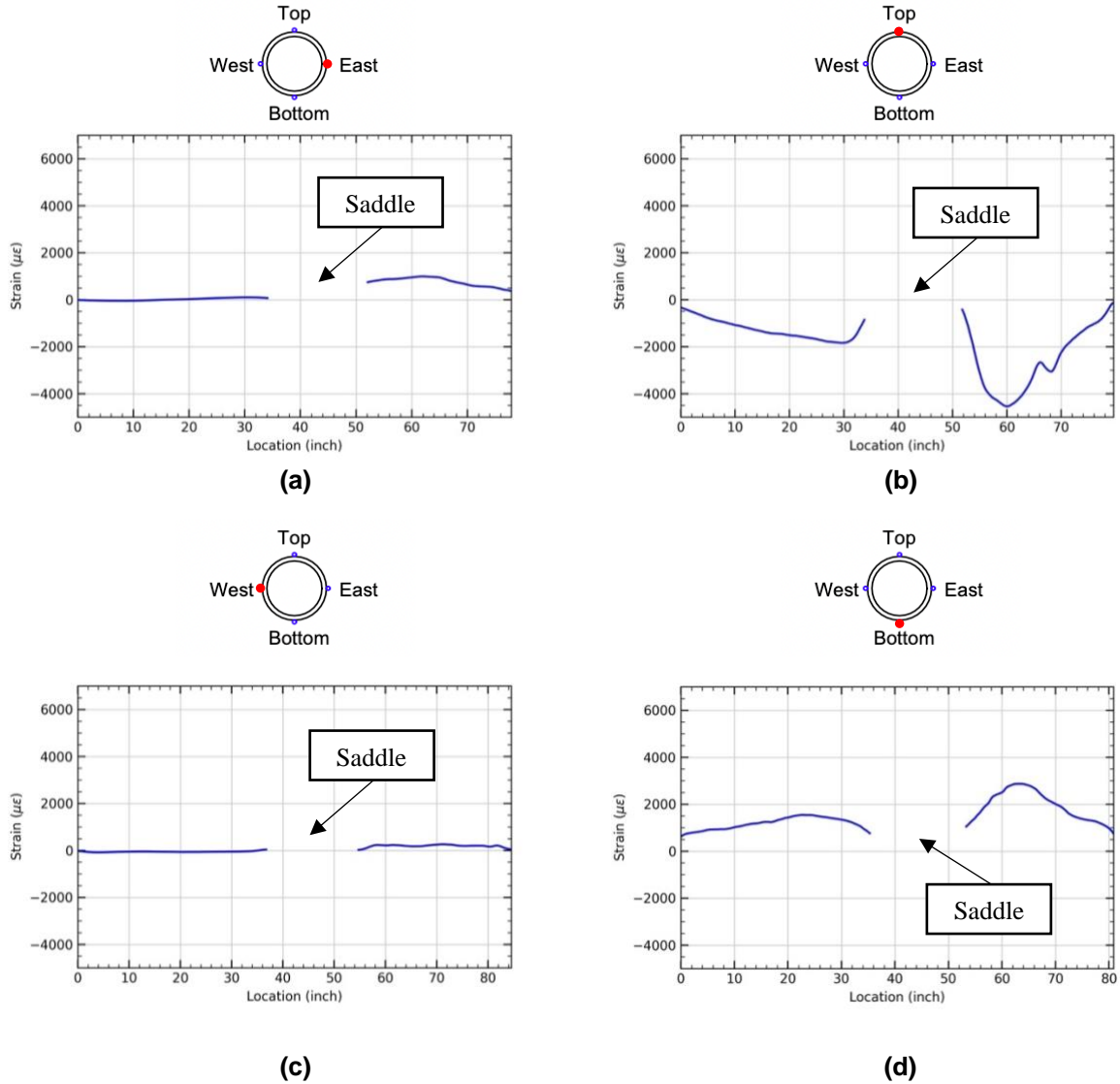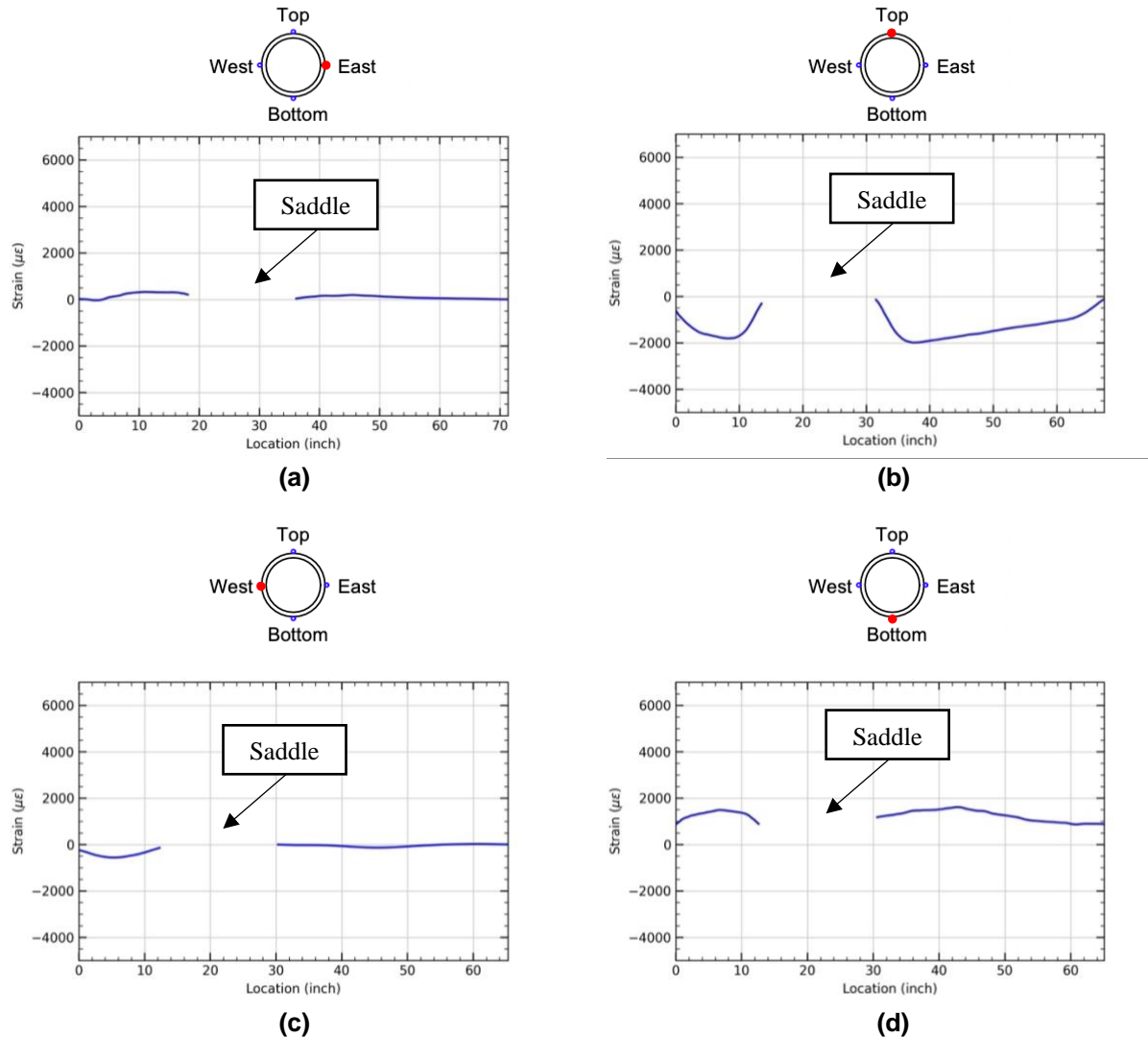

Figure 4-11 Axial strain development of bell pipe of Specimen 2 under 12.5-degree rotation condition. (a) East side, (b) Top side, (c) West side, (d) Bottom side

Figure 4-12 Axial strain development of spigot of Specimen 2 under 12.5-degree rotation condition. (a) East side, (b) Top side, (c) West side, (d) Bottom side

4.2.4 Hoop Strains

The relationships between the hoop strains, measured by strain gauges, and pipe rotation are plotted in Figure 4-13 and Figure 4-14 for Specimens 1 and 2, respectively. Due to Poisson's effect, the strains in the circumferential direction are mainly opposite to those in the longitudinal direction with a smaller magnitude. Again, the large strains in Specimen 2 were due to the out-of-plane rotation and potentially at the location where the spigot bore against the bell invert. Tensile hoop strains can be observed at the "top" and "east,", whereas compressive hoop strains occur at the "bottom" and "west." This indicates that the pipes were squatting. A clear mechanism of the pipe deformation is provided in the following section using the DFOS data.
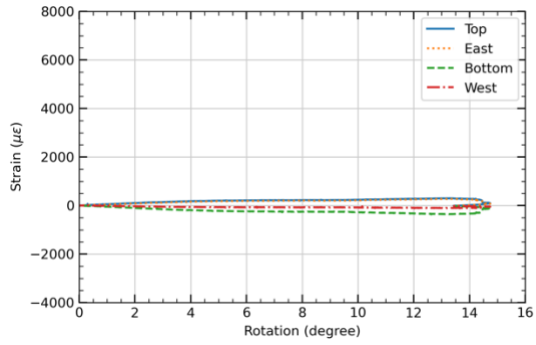
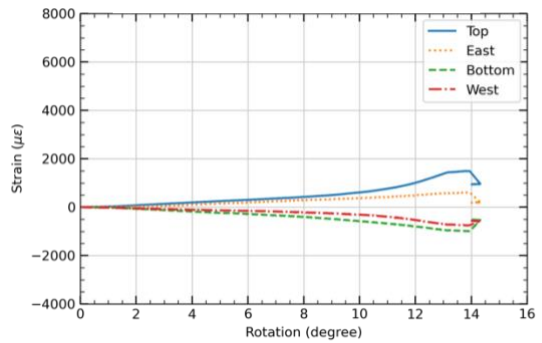(a) Bell Pipe (North)
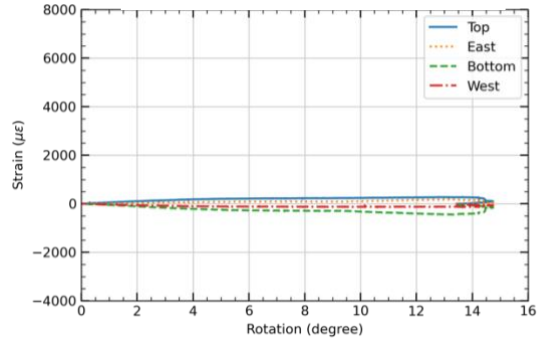
(b) Bell Pipe (South)
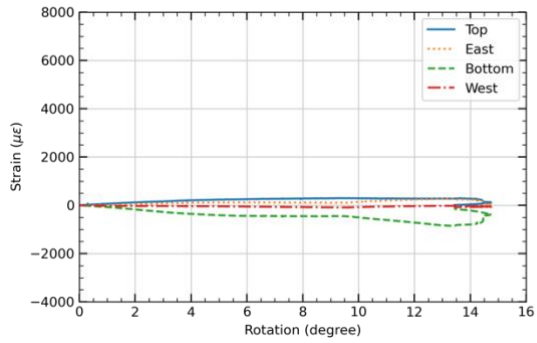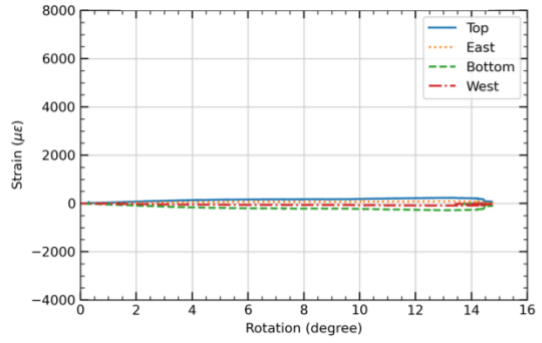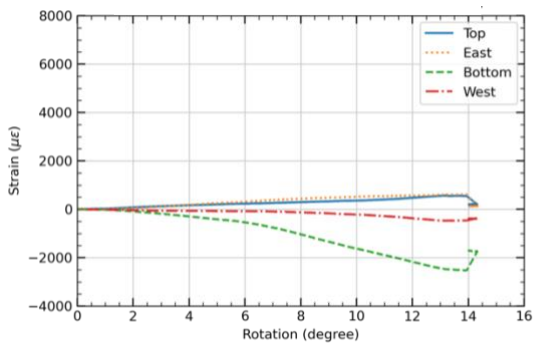
(c) Spigot (North)

(d) Spigot (South)

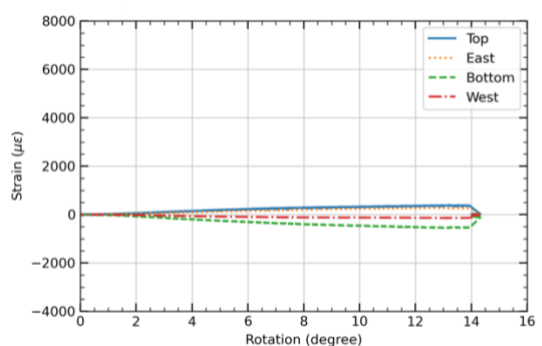**Figure 4-13 Hoop strain vs. rotation of Specimen 1**
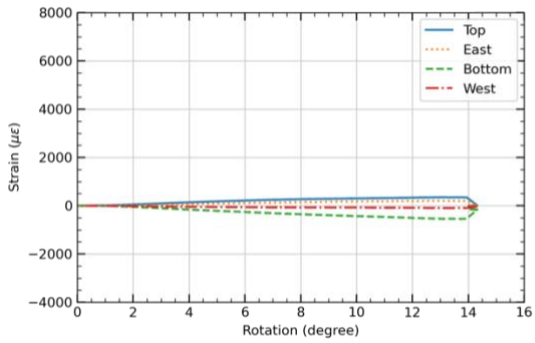
(a) Bell Pipe (North)

(b) Bell Pipe (South)

(c) Spigot (North)

(d) Spigot (South)

Figure 4-14 Hoop strain vs. rotation of Specimen 2

28

The hoop strain results measured from Specimen 1 are plotted in Figure 4-15. The figure shows the results measured by the sensors placed on the bell end (F5), middle of the bell (F6), and on top of the locking segments (F7). Sensor F8 on the spigot was the circumferential sensor closest to the bell. Results of F5 and F8 show that the top side (12 o'clock) is expanding, and the bottom side (6 o'clock) is compressing, indicating the pipes are squatting eccentrically during bending. A similar phenomenon can be found on the other circumferential sensors placed on the pipes (i.e., F1-F4 and F8-F11). The results are documented in Appendix B.
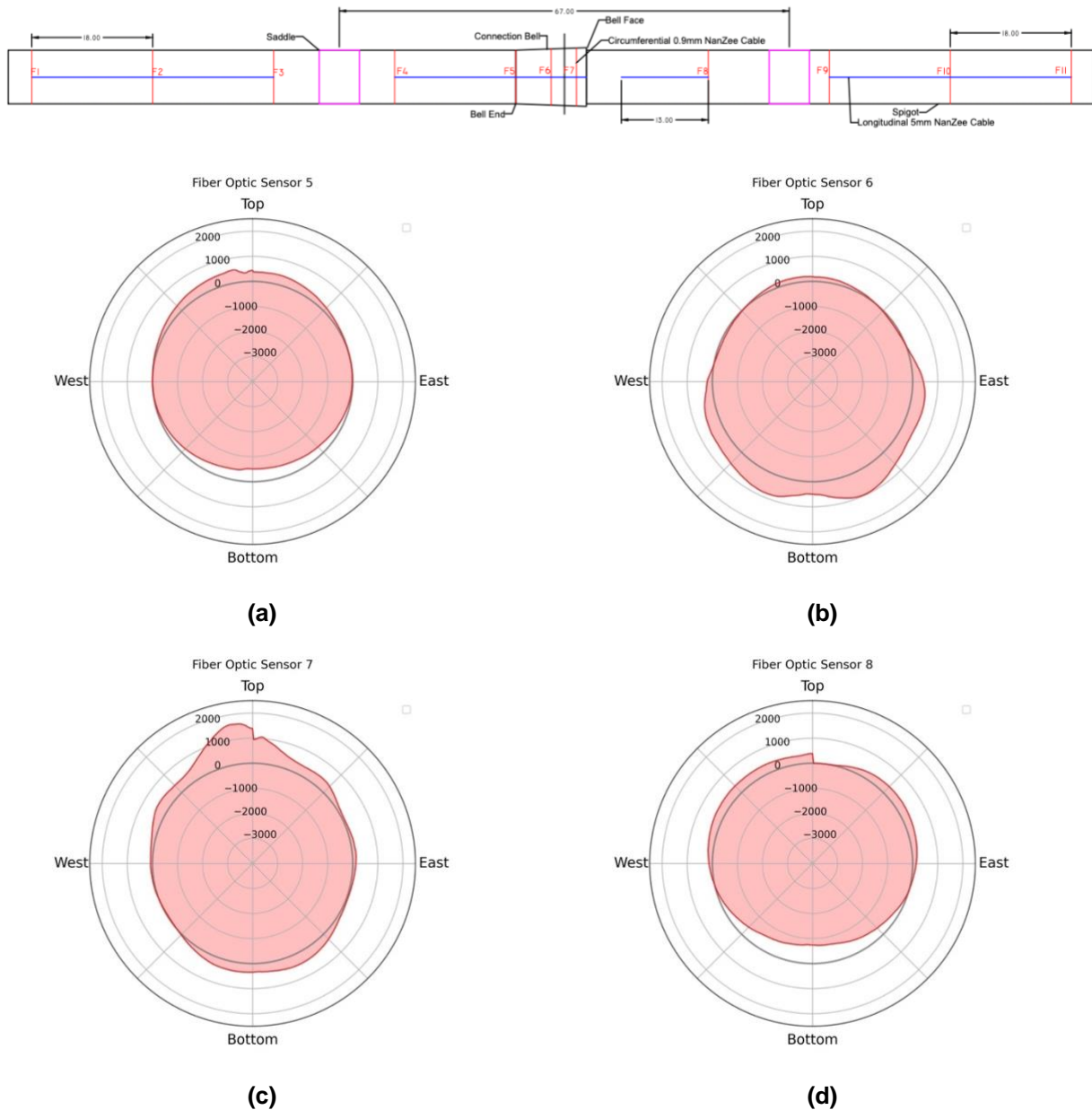
Figure 4-15 Strain distribution in the circumferential direction of Specimen 1 under 12.5-degree rotation condition. (a) sensor on the bell end (b) sensor on the middle of the bell (c) sensor on 3.5-inch away from the bell face (d) sensor on the spigot about 18-inch away from the bell face

The two sensors placed on the bell (F6 and F7) show different patterns. Sensor F6 showed that the bell was expanding on the bottom (12 o'clock). At the locations near the middle of the bell, the spigot was bearing against the bell invert while being pushed down, resulting in expansion on the bottom of the bell. On the other hand, sensor F7 indicated that the bell was squatting, expanding on the top and bottom (6 and 12 o'clock) and shrinking on the other sides (3 and 9 o'clock). The expansion on the bottom side was due to the spigot sitting on the bell invert. On the top side (12 o'clock), the spigot was contacting the bell crown, expanding the top side. The schematic of the mechanism is shown in Figure 4-16.
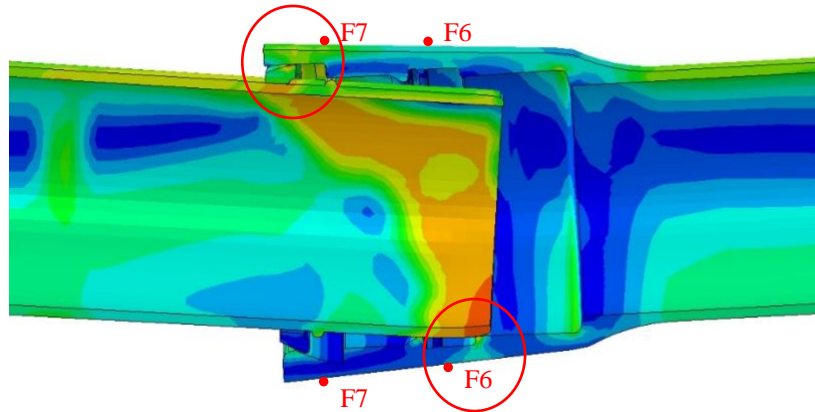

Figure 4-16 Sketch of the mechanism of the bell

Figure 4-17 shows the hoop strains measured in Specimen 2. A similar pattern of strains can be found on the pipes (i.e., F1-F4 and F8-F11) with larger strain values than Specimen 1. The top side (12 o'clock) was under compression, whereas the bottom side (6 o'clock) was under tension. Small strains were found on the other sides (3 and 9 o'clock). As mentioned in the previous sections, the difference in the location where the spigot inside the bell was sitting might be the reason for this strain magnitude difference.

On the bell, a rotation was observed, as shown in Figure 4-17 (a) – (c). The strain distribution in Specimen 1 was merely symmetric along the top-bottom axis. However, the symmetric center line of the strain distribution of Specimen 2 was about 20 degrees offset from the top-bottom axis toward the west side. The phenomenon is due to the non-symmetric locking segment orientation. On the west side (9 o'clock), a rubber gasket was placed instead of having a locking segment, providing less restraint. Therefore, an out-of-plane rotation occurred during the test. Expansion can be found on the top and bottom sides of the bell (F6 and F7) because the bottom of the spigot was bearing against the bell invert, and the crown of the bell face was contacted with the spigot. All the hoop strain results can be found in Appendix B.
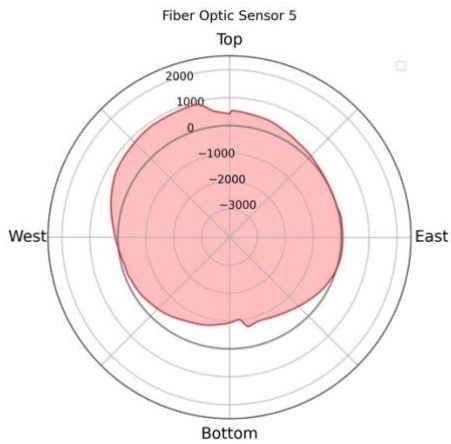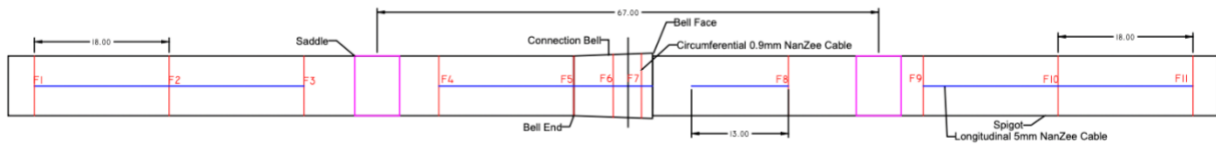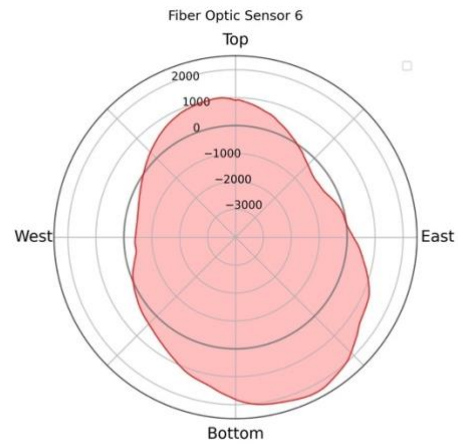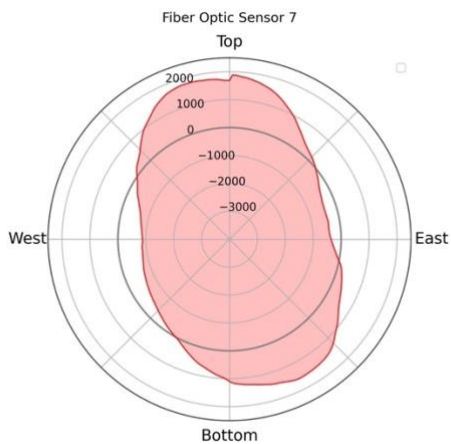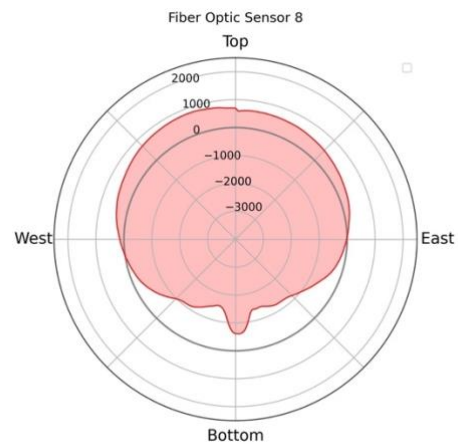
Figure 4-17 Strain distribution in the circumferential direction of Specimen 2 under 12.5-degree rotation condition. (a) sensor on the bell end (b) sensor on the middle of the bell (c) sensor on 3.5-inch away from the bell face (d) sensor on the spigot about 18-inch away from the bell face

5. Finite Element Analysis

5.1 Overview of Numerical Model

Two explicit three-dimensional (3D) full-scale finite element (FE) models were developed using ABAQUS to examine the pipe behavior due to bending force. The geometry and material of the pipe and joint models were carefully designed to be consistent with the experiments. The only difference between the two FE models is the orientation of the locking segments (12 o'clock and 9 o'clock).

In the models, the pipes are simplified into four main parts: a spigot, a bell pipe, three pieces of locking segments and two saddles. The FE mesh used for the analysis is shown in Figure 5-1. The isotropic 3D solid continuum elements (C3D8R) are used. The finer mesh at the bell section is adopted to ensure that strain development can be accurately evaluated. The number of elements and nodes in the pipeline model are 126,227 and 164,803, respectively.
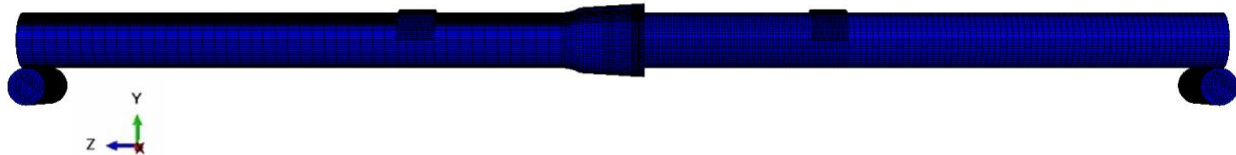

Figure 5-1 3-D FE model mesh for 4-point bending tension tests

The loading conditions and boundary conditions are briefly summarized as follows. At the bell joint, the interaction between the pipe and the locking segments was set to be contacted and allowed to slip between each other. The normal behavior of the interaction was set to behave as the hard contact in ABAQUS, and the friction coefficient of the tangential behavior was imposed as 0.8 according to the standard friction coefficient between materials of ductile iron and steel. In the model, two ends were supported to be allowed to move horizontally and rotate in the yz plane, the same as the boundary condition in the experiment.

The whole process of the FE simulation follows the experimental procedure. Firstly, 50 psi water pressure was applied on the inside surface of the pipe. Then the analysis began with the pipe installed at a fully extended position, where the spigot weld bead contacted with locking segments, as shown in Figure 5-2. Next, the pressure perpendicular to the two saddles was applied to introduce rotations to the specimen.
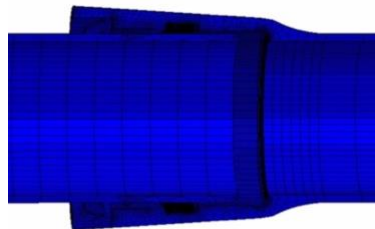

Figure 5-2 FE mesh for bell joint and initial position of the bell and spigot

32

5.2   Determination of Pipe Parameters

Table 5-1 presents the material properties provided by U.S. Pipe for the ductile iron pipe and locking segments used in the tests. The plastic properties were included in the simulation to accommodate some parts of the pipe reaching the yielding stress of the material, resulting in plastic deformation.

Von Mises stress is a value used to determine if a given material yields or fractures in shear. It is mostly used for ductile iron materials. For the tested pipes, when the value of Mises stress exceeded the yield stress (42,000 psi), the pipe generated plastic strains with irreversible deformation. The properties adopted in these FE models are the same as those used for the simulations of the previously reported Tension Tests and Biaxial Tension Tests.

Table 5-1 Ductile iron pipe properties

Part	Density (lb/in^3)	Young's Modulus (psi)	Poisson's Ratio	Yield Strength (psi)	Ultimate Strength (psi)	Elongation
Ductile Iron Pipe (plastic)	0.28	23,500,000	0.29	42,000	60,000	10%
Locking segments (plastic)	0.3	24,000,000	0.26	42,000	60,000	10%

5.3   Overview of FEM Results

Figure 5-3 illustrates the relationship between the moment and rotation of the joint cross-section for both specimens of the whole bending process using FE analysis. At the stage when the pipe is moving downward due to its self-weight, it is found that Specimen 1 (single slot located at 12 o'clock) rotated approximately 5 degrees. However, Specimen 2 (single slot located at 9 o'clock) can only rotate around 4 degrees. During the actuator pushing down stage, both experimental results and FE analysis show that about 13 degrees of rotation is required to fail the specimens regardless of the orientation of the locking segments. The FE analysis reveals that the maximum total rotations (i.e., including self-weight moving down and actuator pushing down stages) and moments are (1) 17.6 degrees with 981.5 kip-in moments for Specimen 1 and (2) 16.2 degrees with 1000.5 kip-in moments for Specimen 2.

Due to the absence of data at the self-weight moving down stage in the experiments, the 0 degree in the experimental results correspond to about 5 degrees and 4 degrees in the FE simulations of Specimen 1 and Specimen 2, respectively. Both experimental and FE analysis results indicate that Specimen 2 requires larger moment than Specimen 1 to achieve a given rotation. The reason might be that Specimen 2 has a locking segment at the top side of the bell while Specimen 1 has a rubber gasket. The ductile iron locking segments provide a more

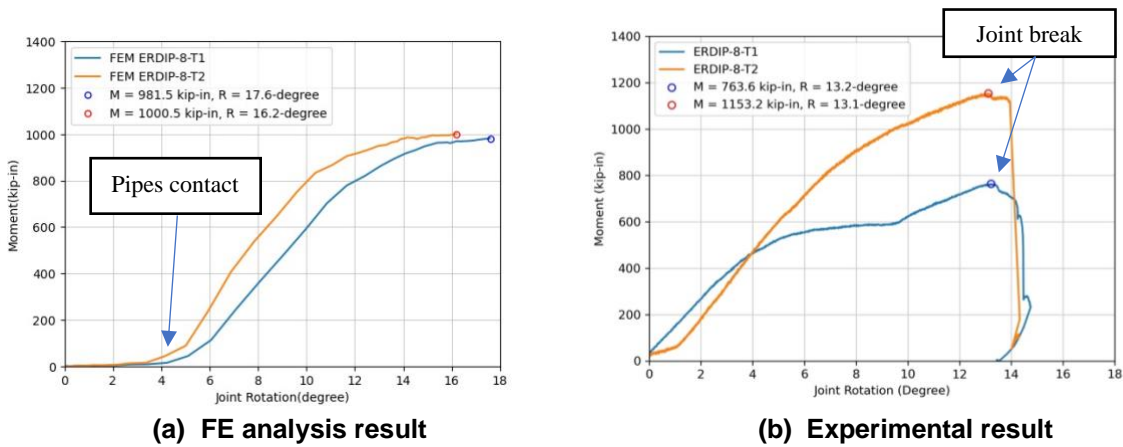resistant force than the rubber gasket, resulting in a more significant moment needed to achieve the desired rotation.

(a) FE analysis result   **(b) Experimental result**

Figure 5-3 Moment and rotation of the specimens

Figure 5-4 shows the Mises stress of the joint under different stages. The joint was initially installed at the fully extended position, meaning that the weld bead on the spigot contacted the locking segments. No significant stress was developed during this stage, as shown in Figure 5-4 (a). Figure 5-4 (b) shows the stage that the bottom of the spigot started to sit on the bedding in the bell. Stresses started to develop for both specimens at the bottom of the spigots. Figure 5-4 (c) depicts the stress distribution at the failure stage. The largest strains were developed at the bottom of the spigot for both specimens, meaning that the bottom of the spigot is the most vulnerable region. Moreover, for Specimen 2, a 45-degree crack started from the bottom of the spigot can be expected.

Specimen 1   Specimen 2
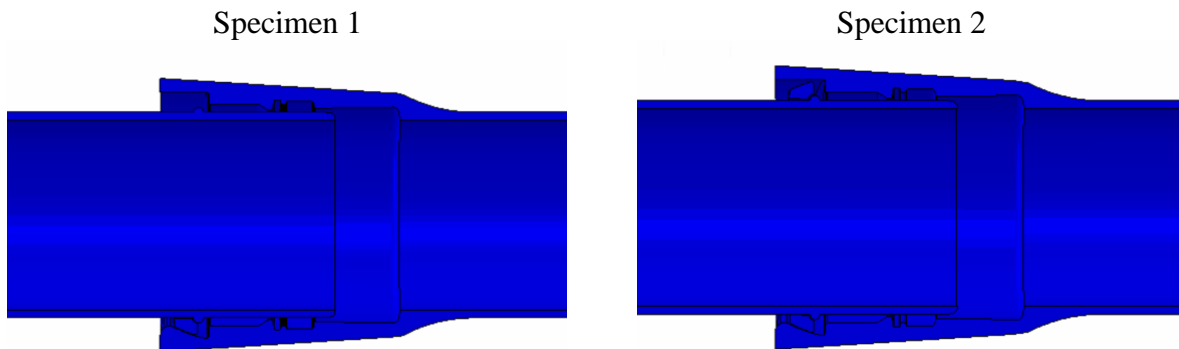
(a) Initial fully extended position
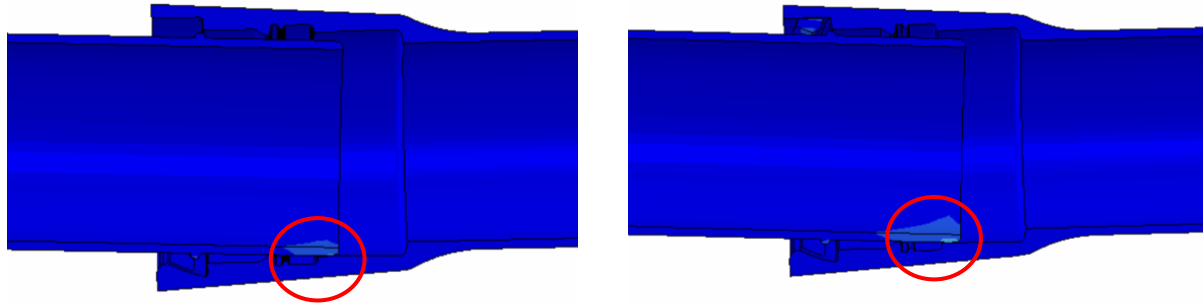
(b) Spigot rotated to contact the bell bedding
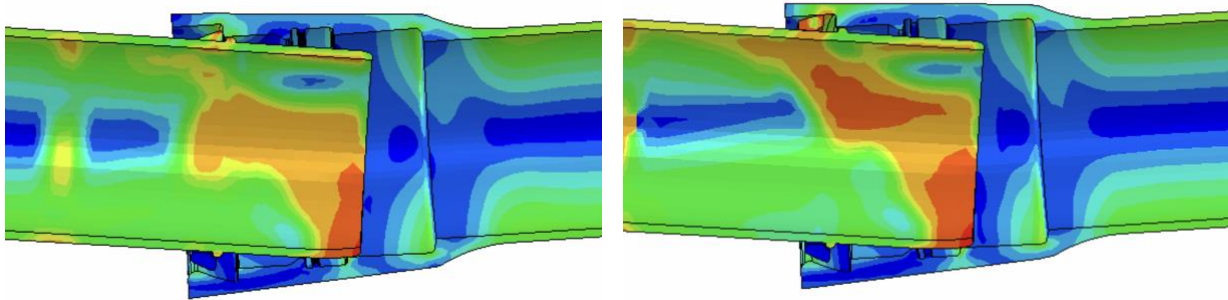
(c) Joint rotated at failure status

Figure 5-4 Joint mechanism under four-point bending force

The moment for a given rotation varies between the experimental data and the FE analysis results, especially the magnitude of the moment in Specimen 1. The results from FEM are larger than that of the test results. This discrepancy could be attributed to the FE models not capturing the effect of the rubber gasket holding the locking segments in place. In the FE models, the rubber gasket is not modeled, meaning that the locking segments located at the sides are allowed to detach slightly and move upwards, as shown in Figure 5-5. Because the locking segments move upward, a certain portion of the spigot is bearing against the locking segment instead of a rubber gasket. This results in a larger moment being generated in comparison to the experimental scenarios where the spigot bears against the rubber gasket on the top. For Specimen 2, however, the locking segment at the top remains at its position. Hence, the phenomenon mentioned above is not observed. Consequently, the moment magnitude differed only slightly from the test results of Specimen 2.

(a) 12 o'clock   **(b) 9 o'clock**
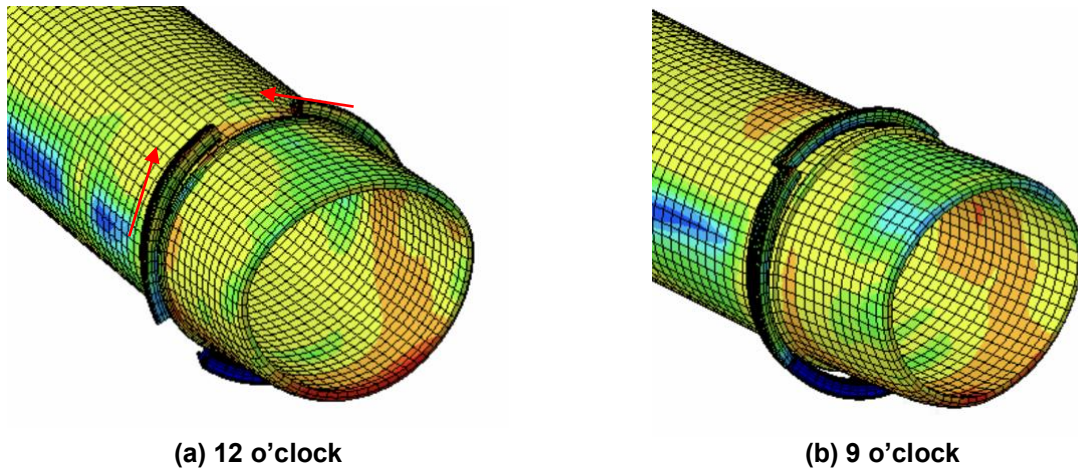
Figure 5-5 Position of locking segments

Due to the different orientations, the Mises stress contours at the joint of the two specimens are different. Table 5-2 compares the Mises stress contours of the spigot at the bottom, top, west and east area for both specimens. A stress concentration can be found at the bottom of the spigot for both specimens, but Specimen 2 has a larger area of large stress concentration than Specimen 1. Also, Specimen 1 has a symmetric stress distribution due to the symmetric locking segment orientation. For Specimen 2, the stresses are not distributed symmetrically. In particular, the east side, without the locking segment, shows higher stress levels, which is why the crack propagated from the bottom to the east side at a 45-degree angle.

Table 5-2 Comparison of Mises stress contour of the joint at spigot area

	Bottom	Top	West	East
Specimen1				
Specimen2				Crack propagation

36

5.4   FEM Results of Specimen 1

5.4.1   Overview of FE Analysis

For Specimen 1, the single slot is located on the top side (12 o'clock), as shown in Figure 5-6. The Mises stress contour and the deformation of the pipeline before-after test are presented.
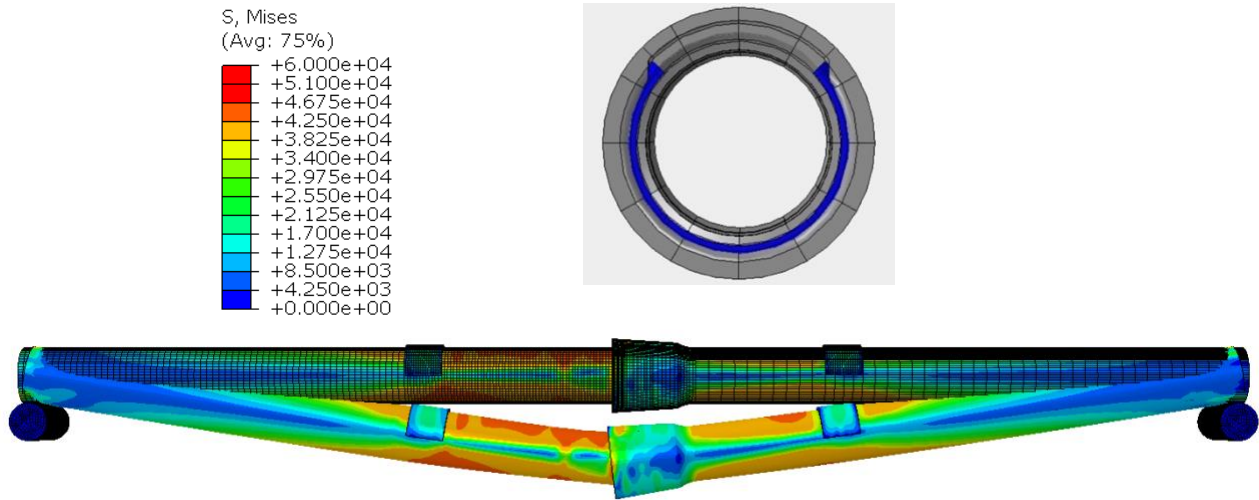
Figure 5-6 Overview of before and after pipeline deformation

The spigot and bell were set to begin with an extended location, as shown in Figure 5-7 (a), where the weld bead of the spigot started to contact the locking segments. Figure 5-7 (b) shows the Mises stress contour and deformation of the joint at the failure stage. Because of the rotation, a significant stress concentration can be found at the bottom of the spigot inside the bell, and the spigot bears against the bell invert. In addition, the locking segment at the bottom was detaching with the weld bead on the spigot and was trying to slip out of the bell.

(a)   **(b)**
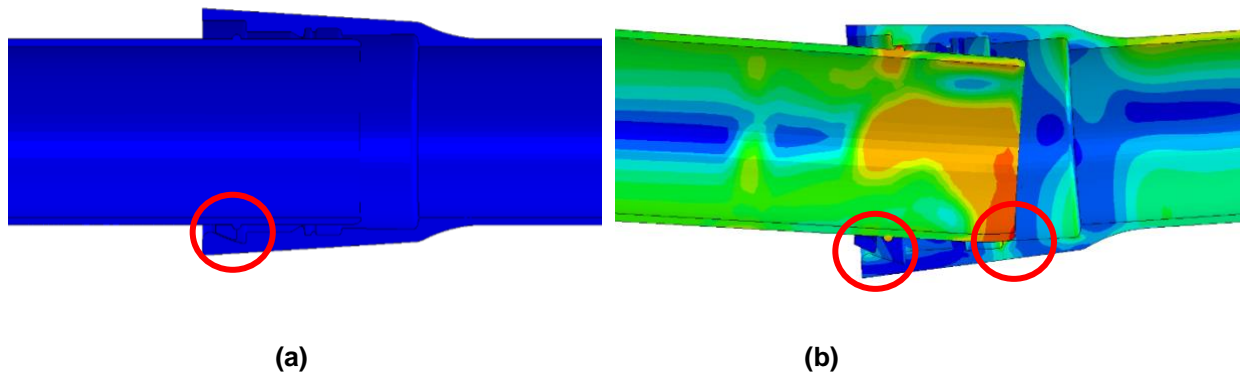
Figure 5-7 Cross-section of joint: (a) initial stage; (b) 10-degree rotation condition

5.4.2 Failure Mode Comparison Between FEM and Experiments

The Mises stress distribution of the joint at the 16-degree rotation condition is shown in Figure 5-8. The result indicates that the stresses distributed in the bell section are generally smaller than those in the spigot. A large stress concentration can be found at the bottom of the spigot. The locking segments were detaching from each other while the specimen was bent. In addition, the bottom locking segment was trying to slip out from the bell. The spigot cross section was squeezed into an ellipse with symmetrical deformation. On the contrary, the shape of the bell remained merely unchanged.

(a)

c

1.8 inch

(b)
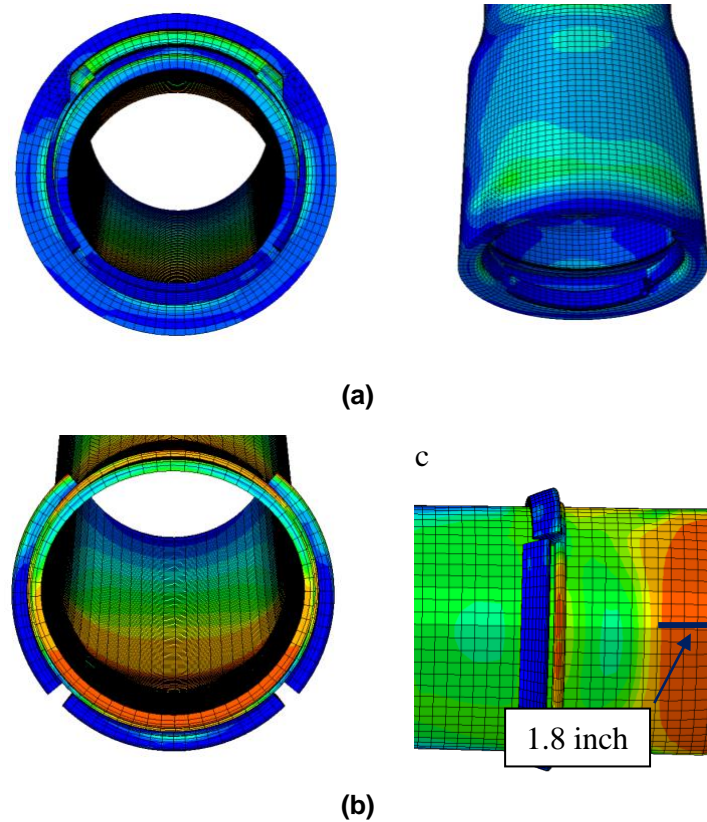
Figure 5-8 The stress contour and deformation of (a) bell (b) spigot

As shown in Figure 5-9, the simulated joint deformation with 3D distributions of Mises stress follows the failure pattern observed in the experiment. The bottom area of the spigot was squeezed to damage. Since the spigot was deformed into an ellipse shape, the west and east sides (3 and 9 o'clock) contacted the internal structure of the bell, resulting in scratches observed on the spigot. The crack at the invert was about 1.8 inches measured from the edge of the spigot, similar to the observation made in the experiment. The maximum principal plastic strains are shown in the colored areas, identifying the areas of significant irrecoverable deformation and potential failure. These numerical results are consistent with the experimental findings.

(a)

(b)
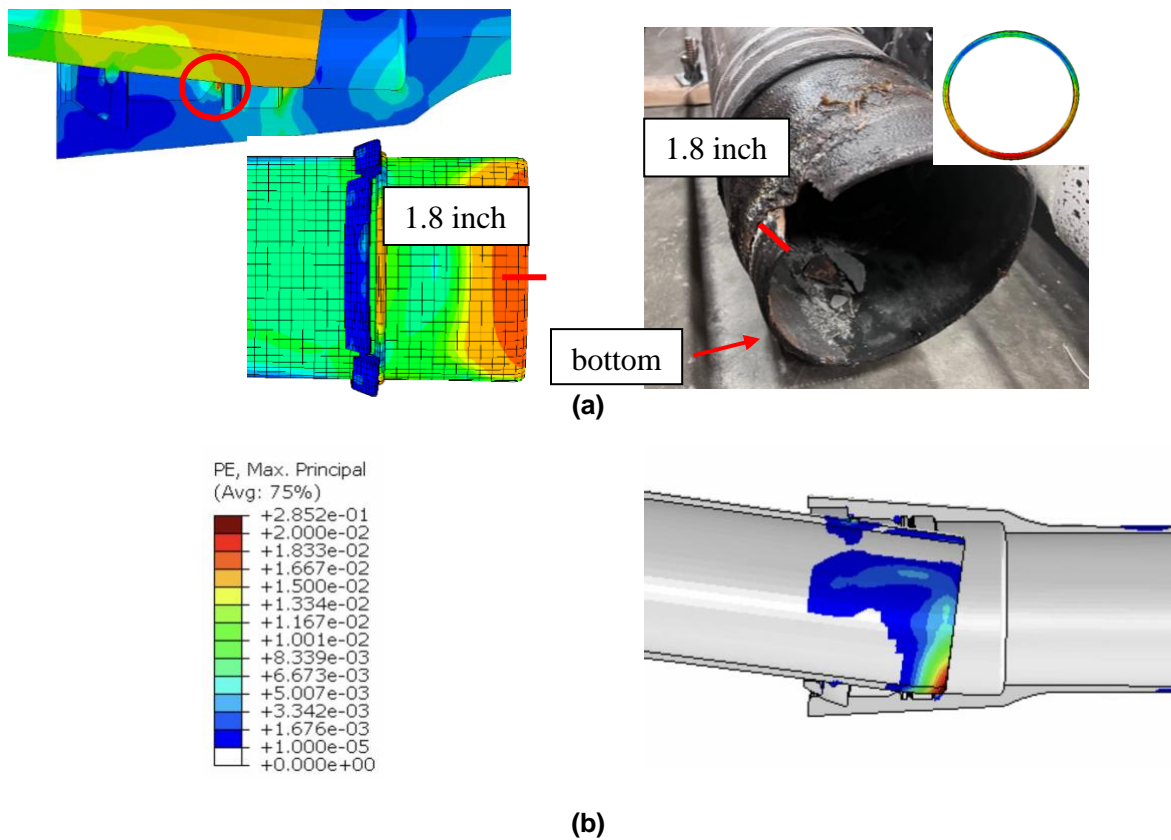
Figure 5-9 Failure pattern comparison: (a) spigot deformation; (b) maximum principal plastic strain distribution

5.4.3 Strain Comparison of the FE Model and Experimental Data

Figure 5-10 and Figure 5-11 show the comparison of the circumferential and longitudinal strain distribution of Specimen 1 in the FE analysis and experimental data when the joint rotation reaches around 13 degrees in the FE model. This condition corresponds to the 8-degree stage in the experiment. The strain results obtained from the FE model match well with the DFOS data, meaning that the FE models can predict the pipeline behavior under the four-point bending conditions.

Sensors F5, F6, and F7 measure the circumferential strains at the bell section, and the data are shown in Figure 5-10. The trend matches well. The difference might be because the locations and pipe material properties in the FE model cannot be perfectly consistent with those in the experiments. The same situation happens in the longitudinal strain comparison.
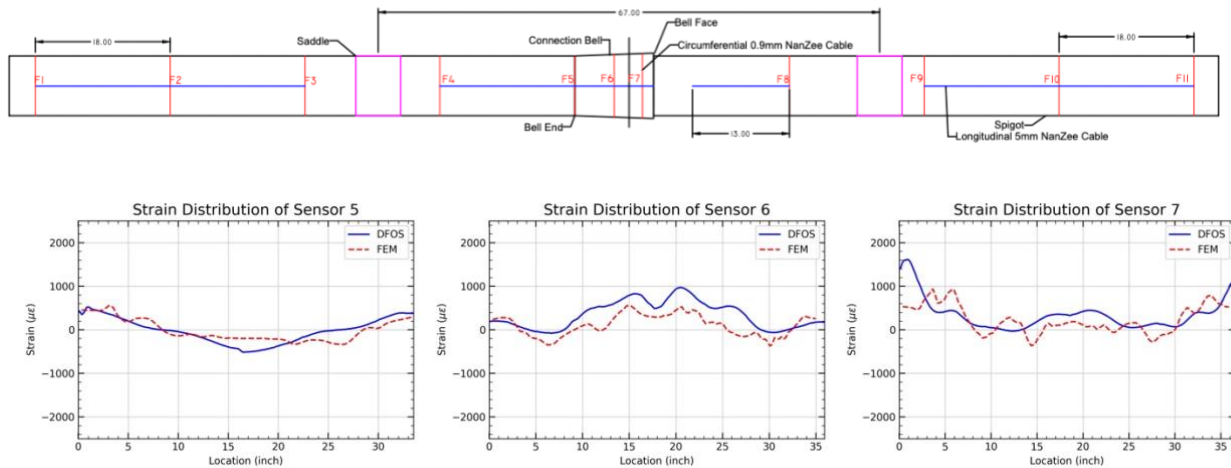
Figure 5-10 Comparison of circumferential strain

Sensors F12, F13, F14, and F15 measure the longitudinal strains at the bell pipe, and the data are shown in Figure 5-11. The gaps of DFOS are the loading saddles. The computed strain values in the FE simulation are larger than those obtained from the DFOSs. The reason might be the sensors used to capture the longitudinal strain in the lab test. The 5-mm diameter cables were used and it has a thicker layer to provide better protection but a less sensitive strain response.

Both FEM results and DFOS data show that strains measured from the east and west (3 and 9 o'clock) were close to zero with minor fluctuations. Similar to the results acquired from the experiments, the top side (12 o'clock) was under compression, and the bottom side (6 o'clock) was under tension.

The difference between the FE and DFOS results may be due to the factor of the loading saddles. Defining the exact loading transfer area between the loading saddle and the pipes in the FE model is difficult. In this study, it is assumed that the areas where the force is transferred are the largest possible contact areas between the loading saddle and the pipe, which might not be the same as in the lab test. More strain comparisons can be seen in Appendix C.

40
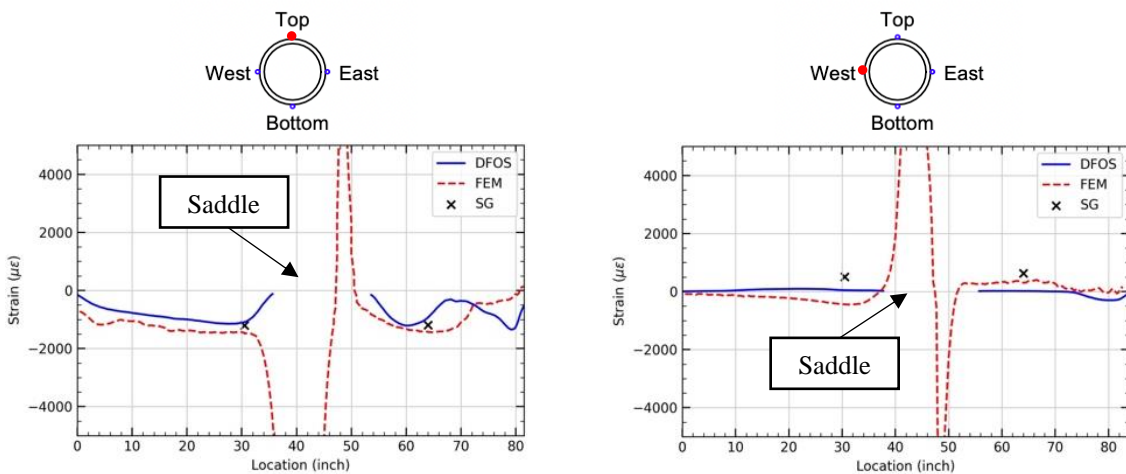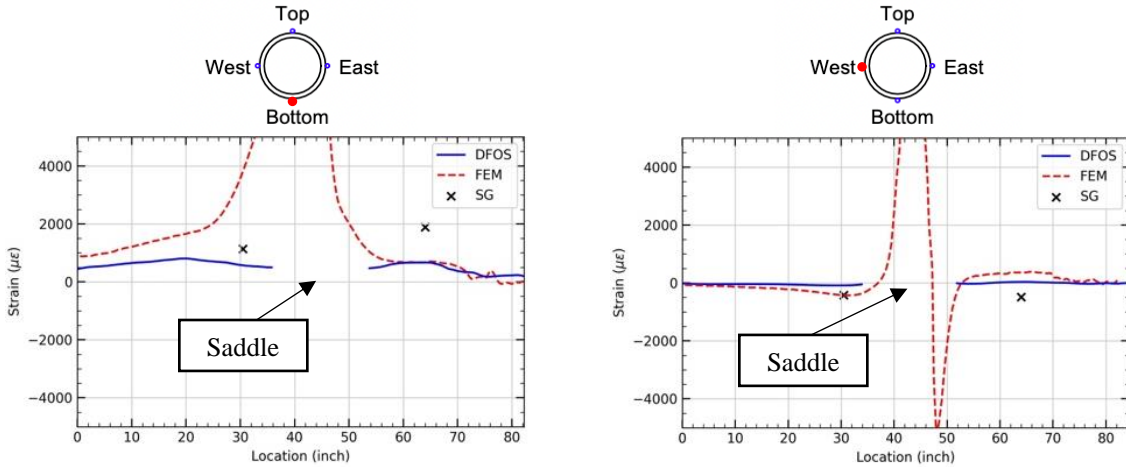
Figure 5-11 Comparison of longitudinal strain

5.5 FEM Results of Specimen 2

5.5.1 Overview of FE Analysis

The only difference between the modeling of Specimen 1 and Specimen 2 is the orientation of the three pieces of the locking segments. The single slot is located on the west side (9 o'clock), as shown in Figure 5-12. The Mises stress contour and deformation of the pipeline before-after test are also shown in the plot.
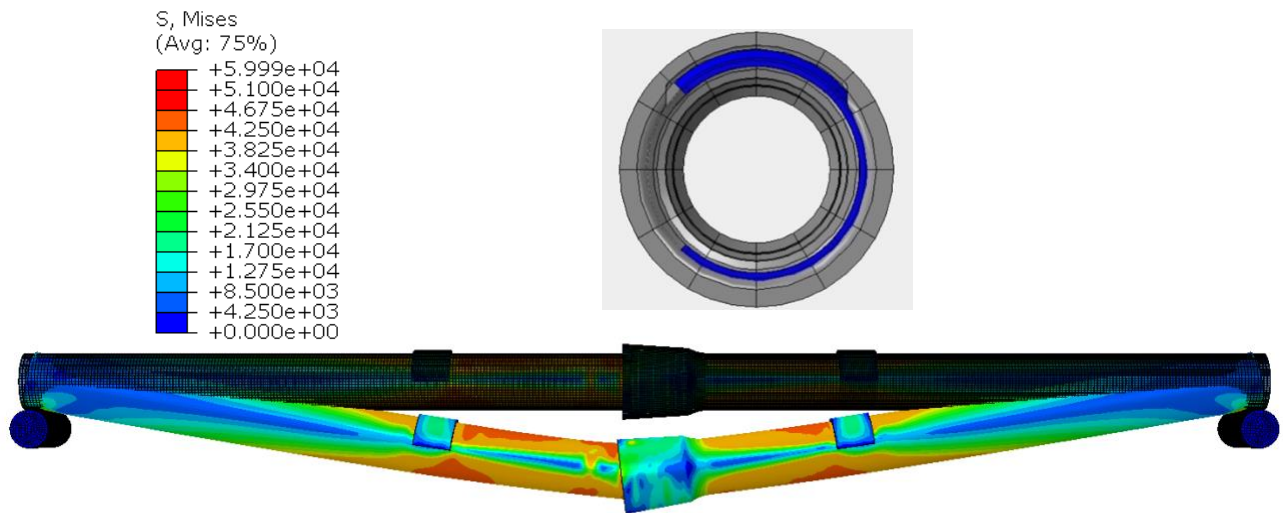
Figure 5-12 Overview of before and after pipeline deformation

The spigot and bell began at the extended position, where the weld bead of the spigot just contacted the locking segments. Figure 5-13 shows the Mises stress contour and deformation of the joint close to the failure stage (16-rotation condition). A significant stress concentration can be found at the bottom of the spigot inside the bell, similar to the observation made in Specimen 1. However, a different stress distribution is observed due to the different locking segment orientations. The locking segment at the bottom also detaches with a weld bead and tries to slip out from the bell, which was also observed in the FE model results of Specimen 1.

(a)   (b)
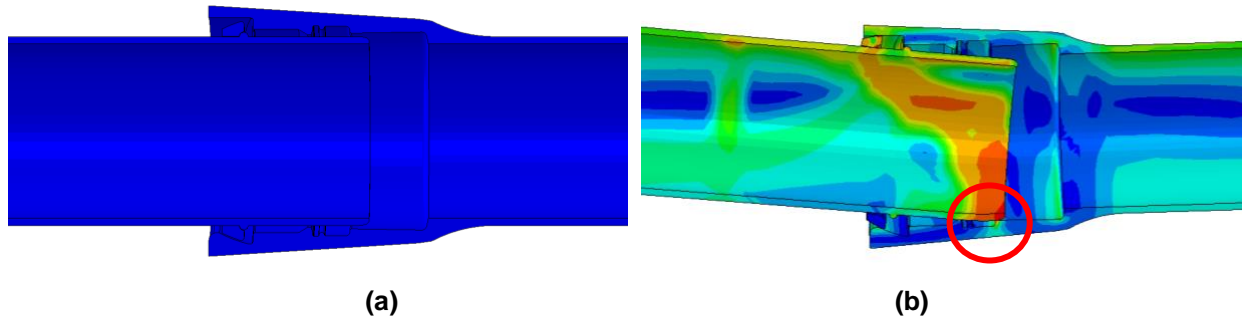
Figure 5-13 Cross-section of joint: (a) initial stage; (b) 10-degree rotation condition

5.5.2 Failure Mode Comparison Between FEM and Experiments

The Mises stress distribution of the joint at 16 degrees of rotation is shown in Figure 5-14. Similar to the observation made in Specimen 1, the stresses distributed at the bell section are generally small compared to those on the spigot. A large stress concentration can be found at the bottom of the spigot. Moreover, the locking segments detach from each other while the specimen is bent. The top and bottom locking segments are trying to slip out from the bell, which differs from what was observed in Specimen 1. The spigot cross-section deforms into an ellipse shape with symmetrical deformation.

(a)

(b)
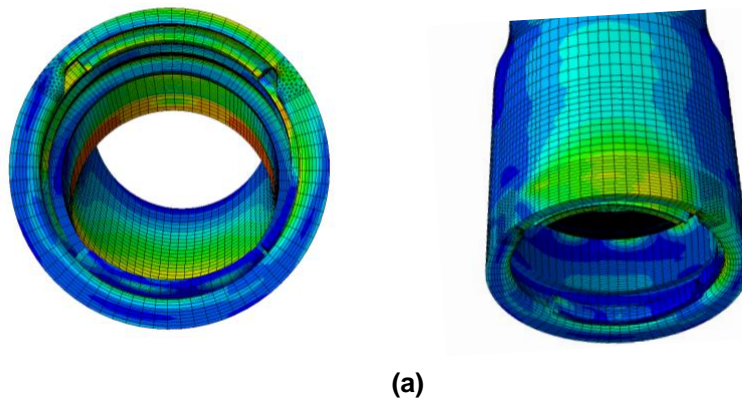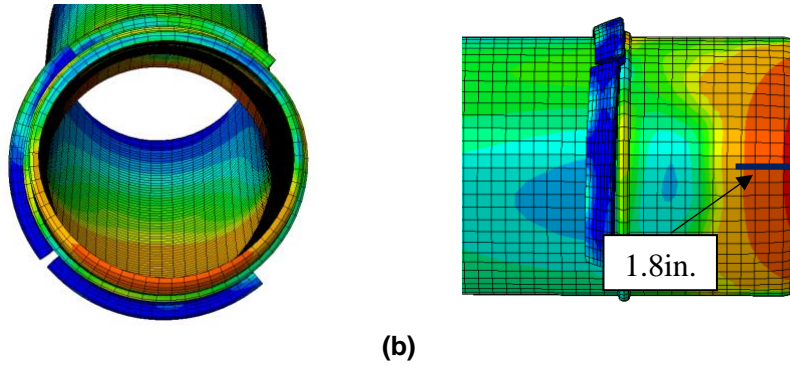
Figure 5-14 The stress contour and deformation of (a) bell (b) spigot

The simulated joint deformation follows the failure pattern of the joint observed in the experiment, as shown in Figure 5-15(a). The bottom of the spigot is squeezed into an ellipse shape and damaged. A 45-degree crack propagates from the west to the back through the bottom. The circumferential crack at the bottom of the spigot is about 1.8 inches from the edge. The maximum principal plastic strains are shown in the colored area in Figure 5-15(b), indicating the areas under significant irrecoverable deformation. The failure mechanism found in the FE model is similar to the observation made in the experiment.

(a)

(b)
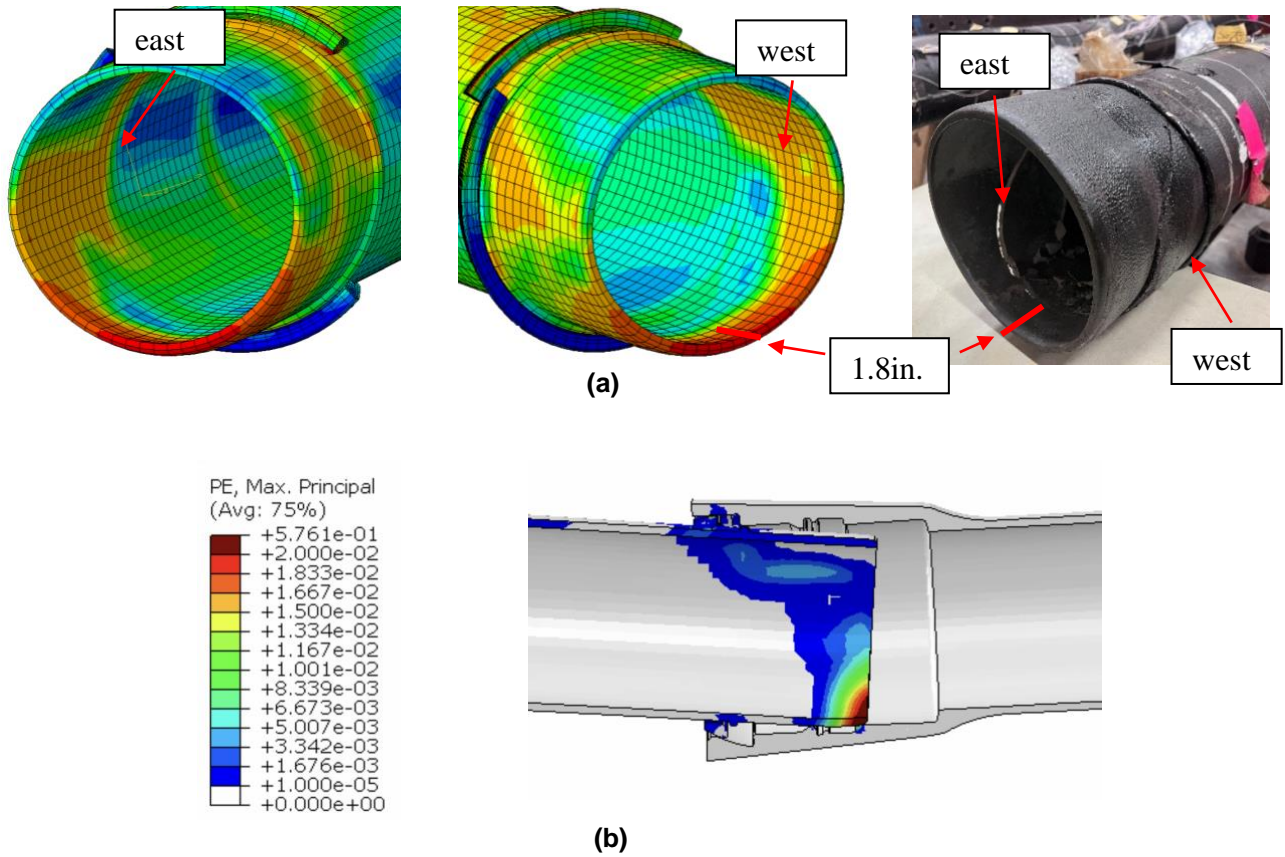
Figure 5-15 Failure pattern comparison

5.5.3 Strain Comparison of the FE Model and Experimental Data

Figure 5-16 and Figure 5-17 show the comparison of the circumferential and longitudinal strain distribution on Specimen 2 between the FE analysis and the experimental data when the joint rotation reaches around 12 degrees of rotation in the FE model. This corresponds to 8 degrees of rotation in the experiment. Sensors F5, F6, and F7 measure the circumferential strains at the bell joint. The trends of the strain distribution measured by these sensors match well between the FE analysis results and DFOS data. However, the magnitudes are different. This may be because, during the lab test, the spigot edge displaced to the bell groove, as shown in Figure 5-18. Besides, the groove area is thinner than the other bell area, representing lower stiffness, which may cause more significant strain distribution and a large possibility of the bell joint failure.
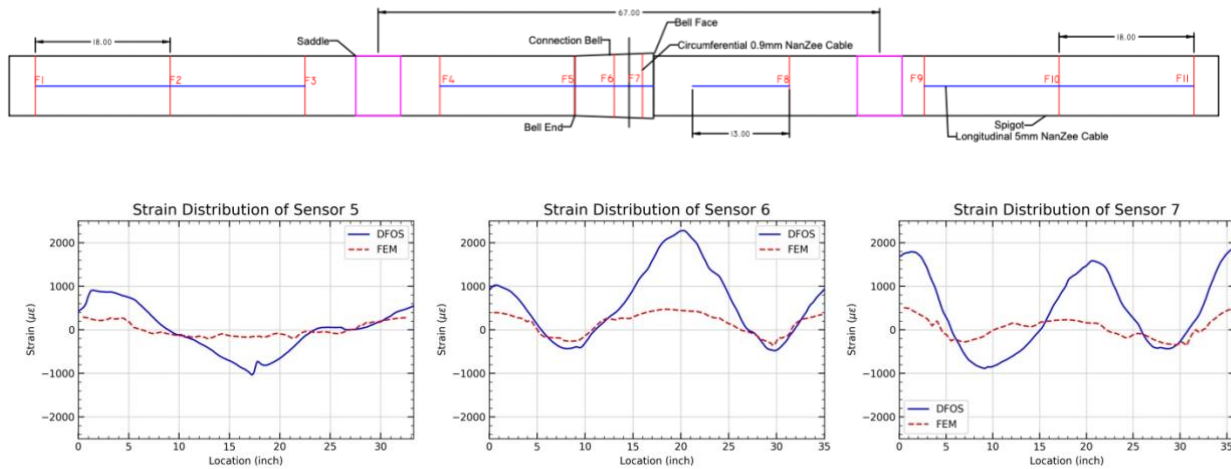
Figure 5-16 Comparison of circumferential strain

The same observation is made for the longitudinal strain results. The DFOS data show a more significant strain than the FE analysis results. The reason may be the same as discussed above. Both FEM results and DFOS data show that the strains from the west and east sides (3 and 9 o'clock) are almost zero, with several fluctuations. Further information on strain comparisons can be found in Appendix C.
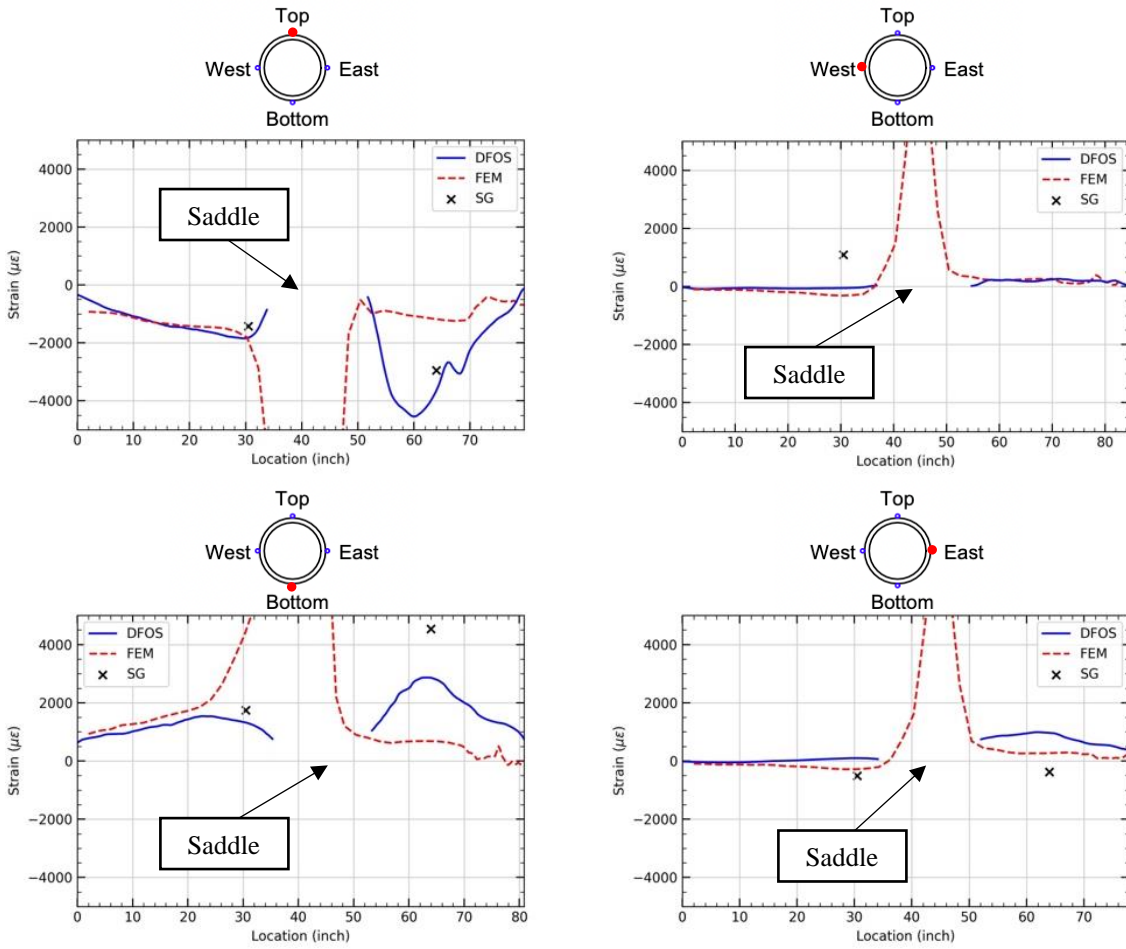
Figure 5-17 Comparison of longitudinal strain
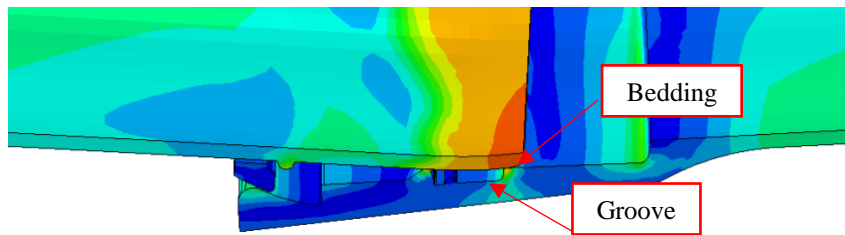
Figure 5-18 Sketch of the mechanism of the bell

6. Conclusion

This report describes the results of the experiments and FE analysis on the performance of an 8-in TR-XTREME^{TM} ductile iron pipe under four-point bending. The results were used (i) to develop the relationship between joint moment and rotation, (ii) to determine the joint rotational capacity, as well as (iii) to discuss the failure mechanism of the two specimens with different locking segment orientations.

The FE simulation results demonstrate a allowable rotation of 5 degrees for Specimen 1 (with the single slot situated at the 12 o'clock position) and 4 degrees for Specimen 2 (with the single slot located at the 9 o'clock position), before the spigot makes internal contact with the bell, which is similar to manufacturer's guideline. Following this, both experimental and FE analysis data reveal that the joint can continue to maintain an approximately 13 degrees of rotation before the joint cracks, regardless of the orientation of the locking segment. This demonstrates that the joint possesses a significant rotational capability, accommodating approximately 17 degrees of rotation prior to joint failure and up to 18 degrees of rotation before the initiation of water leakage for both specimens.

The primary failure occurred at the bottom side of the spigot inserted inside the bell, and no significant damage was found on the bell. Specimen 1 generally required a smaller moment to achieve a given rotation than Specimen 2. Both FE analysis and experiments showed that the weakest area was around 1.8 inches from the edge of the bottom side of the spigot. The stress distribution in Specimen 1 is symmetrical. An out-of-plane rotation is found in Specimen 2, resulting in non-symmetrical stress distribution. This is due to the non-symmetrical locking segment orientation of Specimen 2. The orientation of locking segments may have little influence on the spigot stress distribution but may affect the crack propagation pattern.

In this study, 3D FE models were calibrated with full-scale experiments and were further adopted to analyze the impact of the orientations of the locking segments. The strain distribution and failure patterns matched well between the experimental results obtained from the DFOSs and the simulation, indicating that the proposed FE model can reasonably predict pipe behavior under the four-point bending conditions. The developed FE model can be used for future parametric studies and as a guide for improved pipe design.

7.Reference

U.S. Pipe. (2020). TR XTREME [Brochure]. https://www.uspipe.com/wp-content/uploads/2020/12/USP_TR_XTREME_Brochure_03-03-2020-for-web.pdf?fbclid=IwAR2n950mDSY8OQ39WFCoVzV8WWoNmk_ae88eCPNjQym1okpuRK7mLp6absE

LUNA inc. (2022). ODiSI 6000 Series Optical Distributed Sensor Interrogators. Retrieved from https://lunainc.com/sites/default/files/assets/files/data-sheet/Luna%20ODiSI%206000%20Data%20Sheet.pdf

Wu, J., Jiang, H., Su, J., Shi, B., Jiang, Y., & Gu, K. (2015). Application of distributed fiber optic sensing technique in land subsidence monitoring. Journal of Civil Structural Health Monitoring, 5(5), 587-597.

ABAQUS. (2020). https://www.3ds.com/support/hardware-and-software/simulia-system-information/abaqus-2020/

Appendix A: Distributed Fiber Optic Sensing

Using the physical properties of light, fiber-optic sensing can detect changes in temperature, strain, and other parameters when light travels along a fiber, which uses fiber-optic cables as sensors and can measure over long distances at 100 to 1000s of points on a single cable or multiplexed cables depending on the analyzer used. Compared to the other sensing technologies, fiber-optic sensing has distinct advantages such as small size, light weight, and strong resistance to corrosion and water. Distributed fiber optic sensing consists of two main components, an analyzer, and fiber-optic cables. LUNA ODiSI 6000 series integrator was used as the analyzer, and NanZee Sensing Technology Co manufactured the fiber-optic cables in the experiments.

LUNA Interrogator
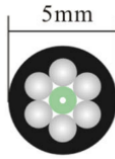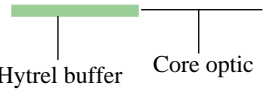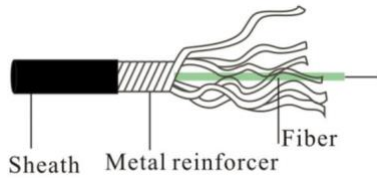
Figure A-1. LUNA ODiSI 6000 Series optical distributed sensor interrogator (LUNA, 2022)

LUNA ODiSI 6104 is an optical distributed sensor interrogator that can provide thousands of strain or temperature measurements per meter of a single high-definition fiber sensor. High-Definition H.D.D) Sensors - Strain & Temperature (HD-SC) temperature sensors utilize an advanced interrogation mode of the ODiSI to increase the accuracy of measurements when the sensors are subjected to strain, such as in embedded and surface-mount installations. It can achieve a sensor gauge pitch (the distance between two measurement points) as small as 0.65 mm, a sensor length of up to 50 m, and a measurement rate of up to 250 Hz with an accuracy of less than ±1 microstrain.

Fiber-optic Cable

Two types of fiber optic cables manufactured by NanZee Sensing Technology Co. were used; (a) 5 mm diameter armored cable (NanZee 5mm) and (b) 0.9 mm diameter cable (NanZee 0.9mm). Table A-1 lists the information on the cables. The difference between the two cables is the thickness and material of the coating. NanZee, a 5mm cable, provides a sheath layer and steel reinforcement, resulting in better protection to the optical core; hence, it can be used for the actual field application. The coating of NanZee 0.9mm cable is thinner than NanZee 5mm cable. NanZee 0.9mm cable has less protection, but a more sensitive strain response is achieved.

Table A-1 Schematic illustration of the selected strain sensor cable (Wu et al., 2015)

Brand	NanZee Sensing Technology Co.	NanZee Sensing Technology Co.
Model	NZS-DSS-C07	NZS-DSS-C02
Cross section	0.9mm	5mm
Side view	Hytrel buffer Core optic	Sheath Metal reinforcer Fiber

Appendix B: Distributed Fiber Optic Sensors Result

All the results from the distributed fiber optic sensors are demonstrated herein. The strain distributions are plotted when the specimens reach 12.5 degree of rotation.

F5

F6

F7

F8

F9

Fiber Optic Sensor 9

Fiber Optic Sensor 9

F10

Fiber Optic Sensor 10

Fiber Optic Sensor 10

F11

Fiber Optic Sensor 11
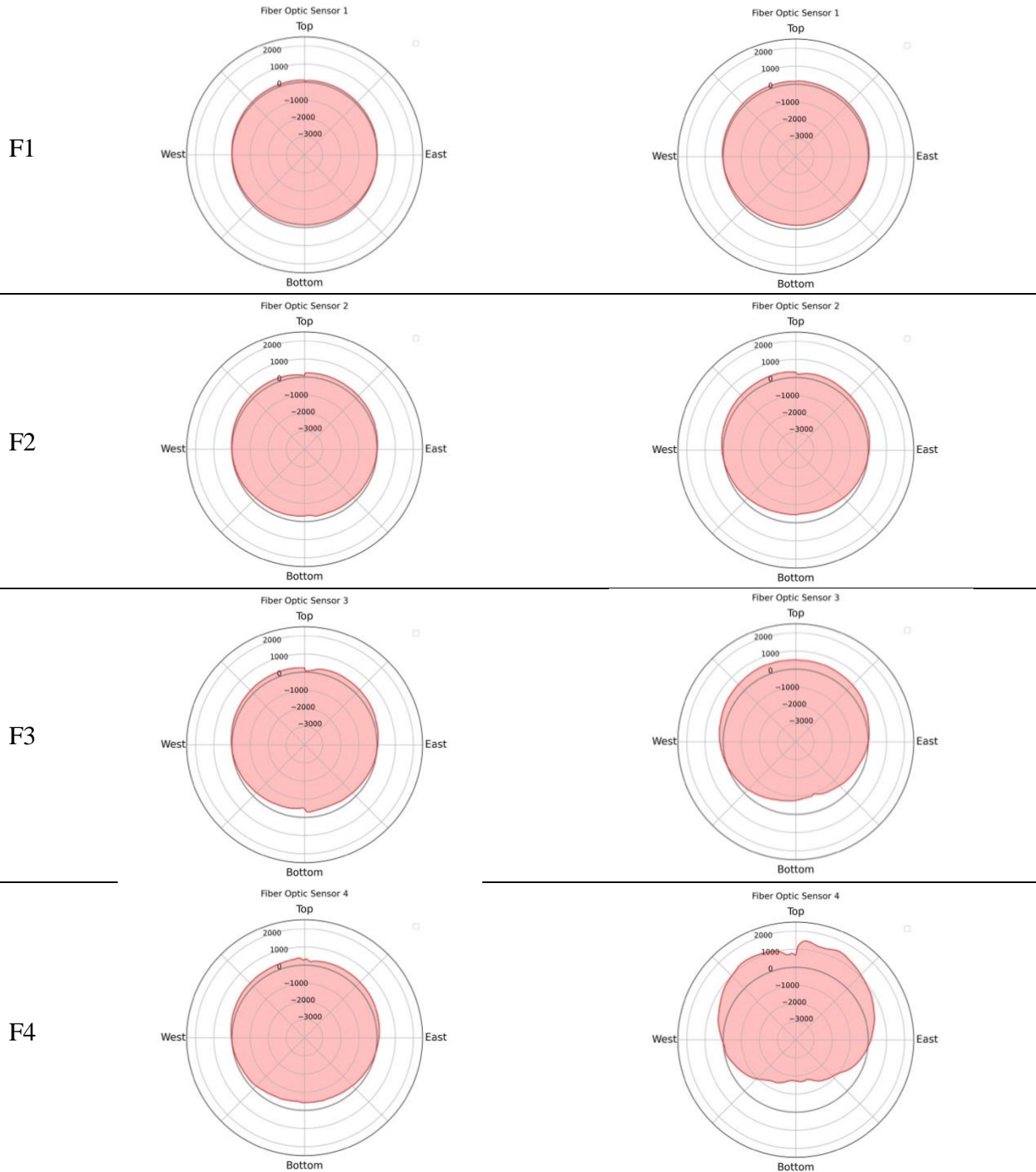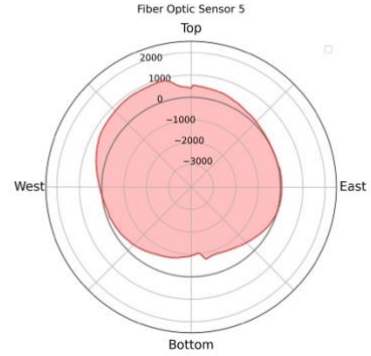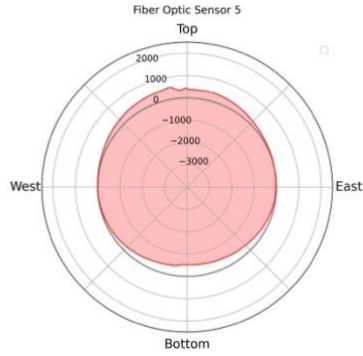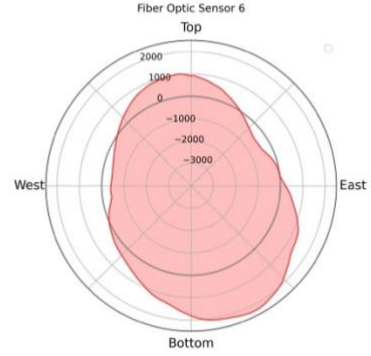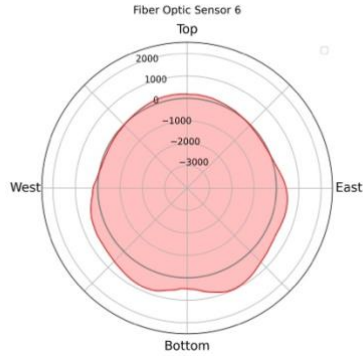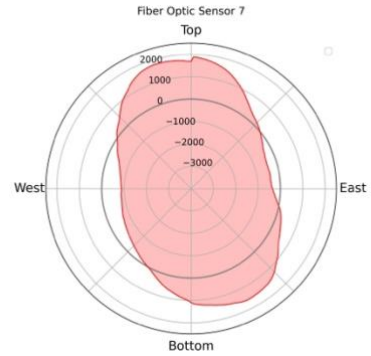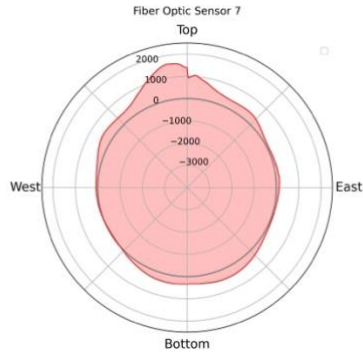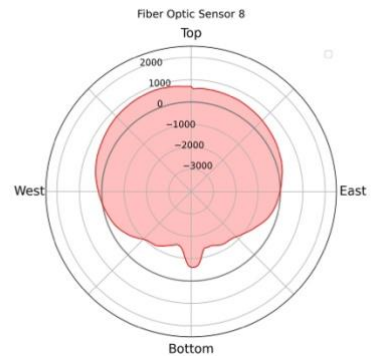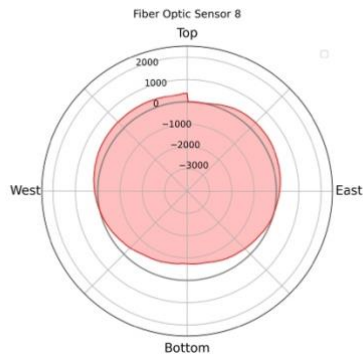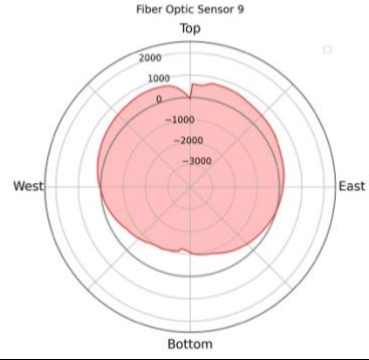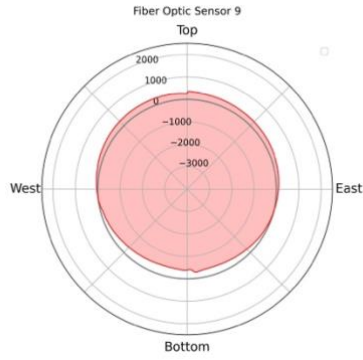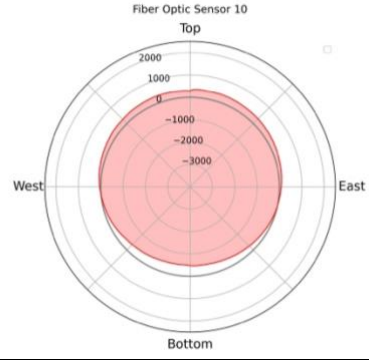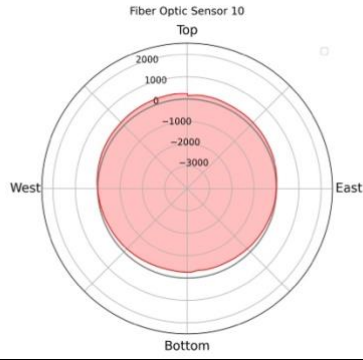
Fiber Optic Sensor 11
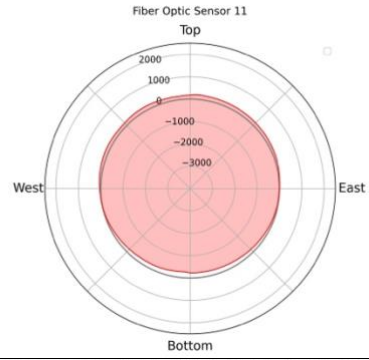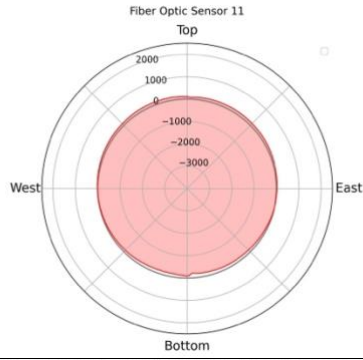
F12
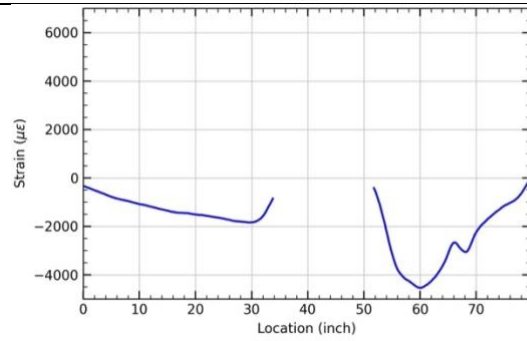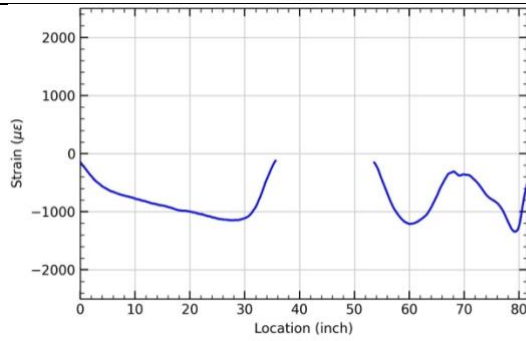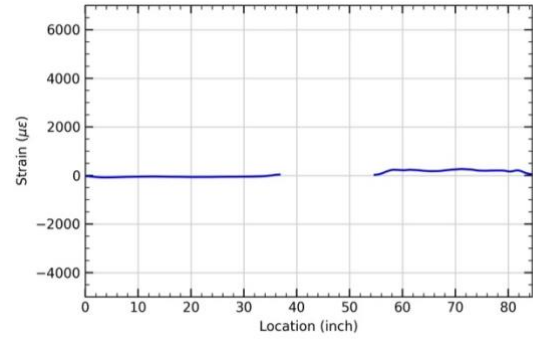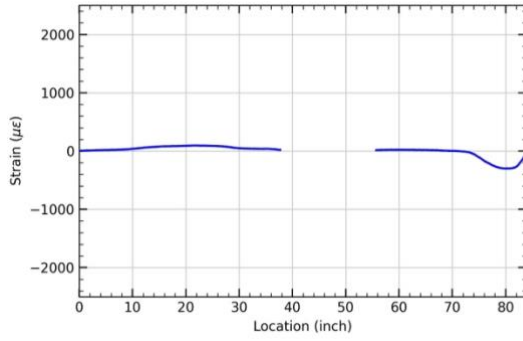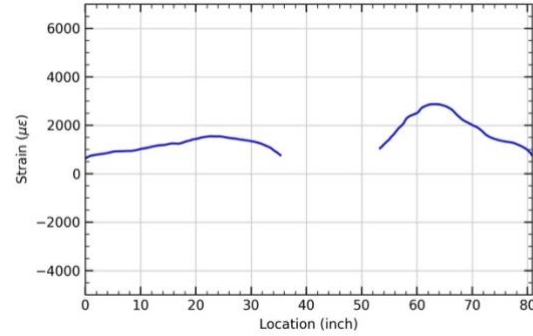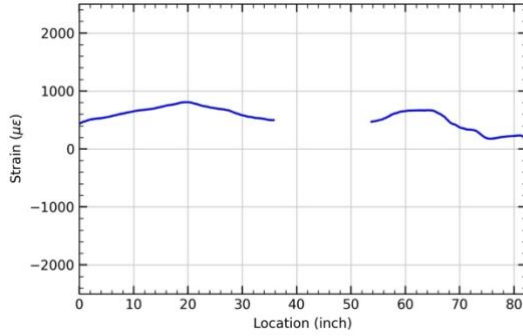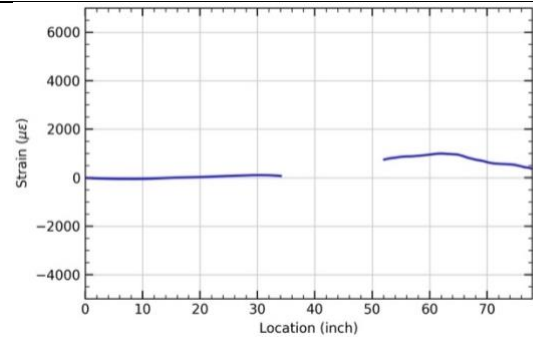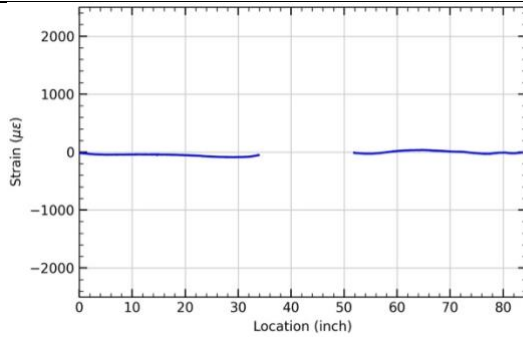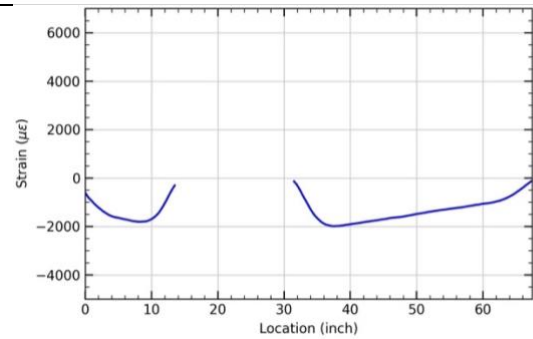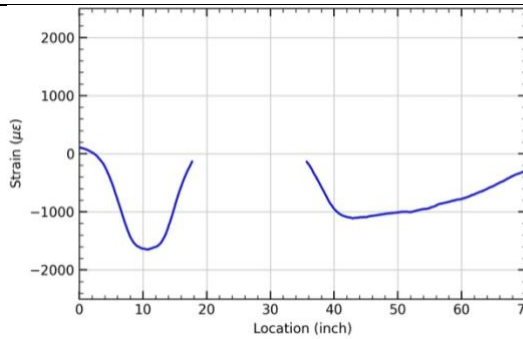
F13
F14
F15
F16
F17
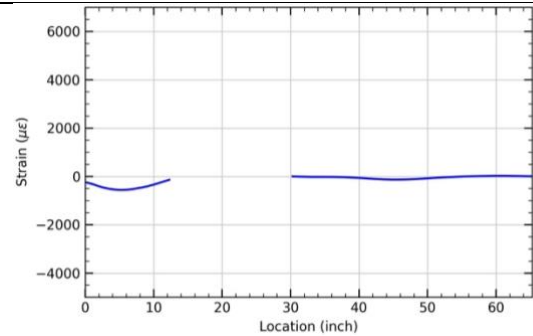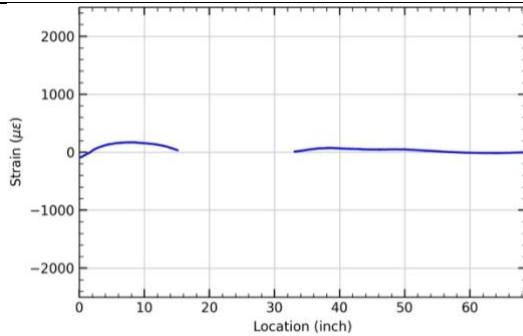
F18
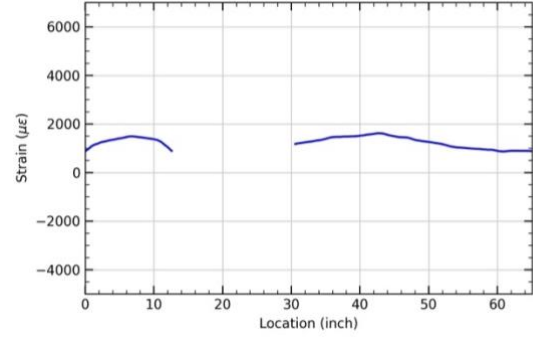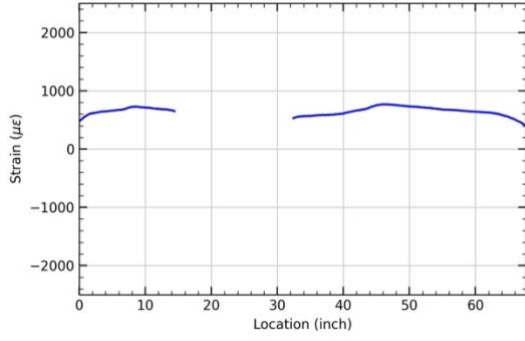
F19
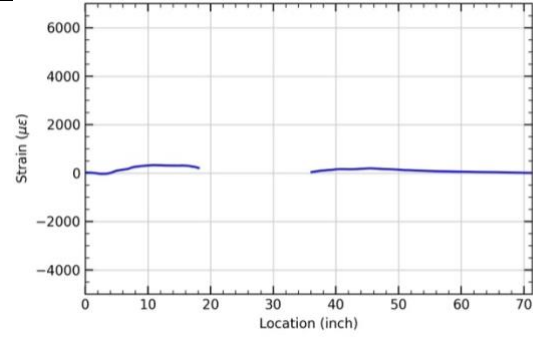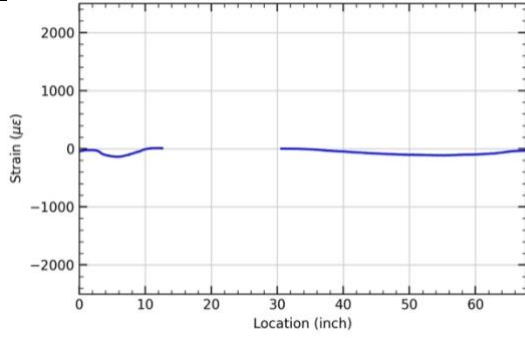
(a) Test 1   (b) Test 2

Appendix C: Comparison of FEM simulation results and experimental results

The experimental data were compared to the results from the FE model. All the comparison results are shown in this section.
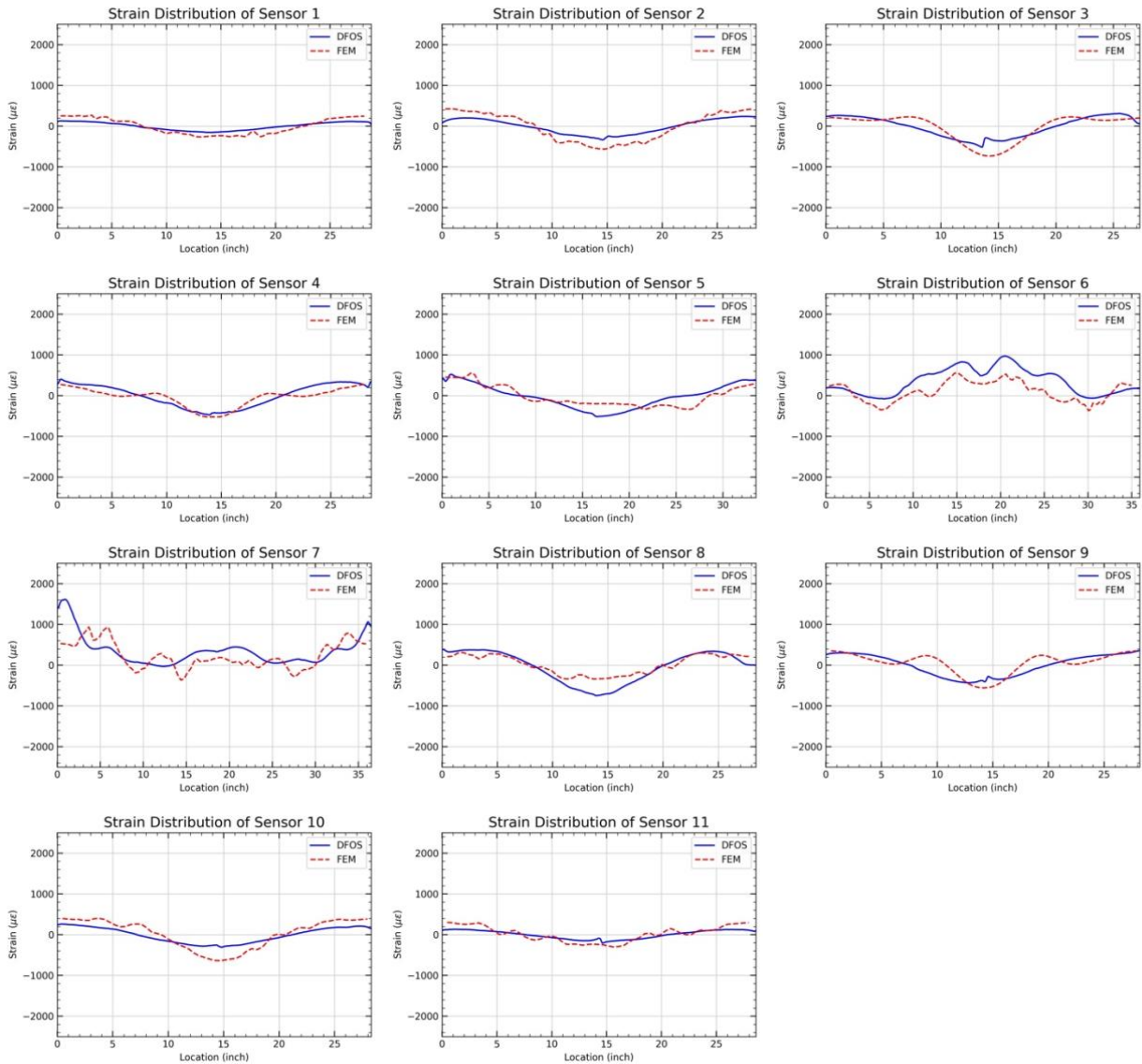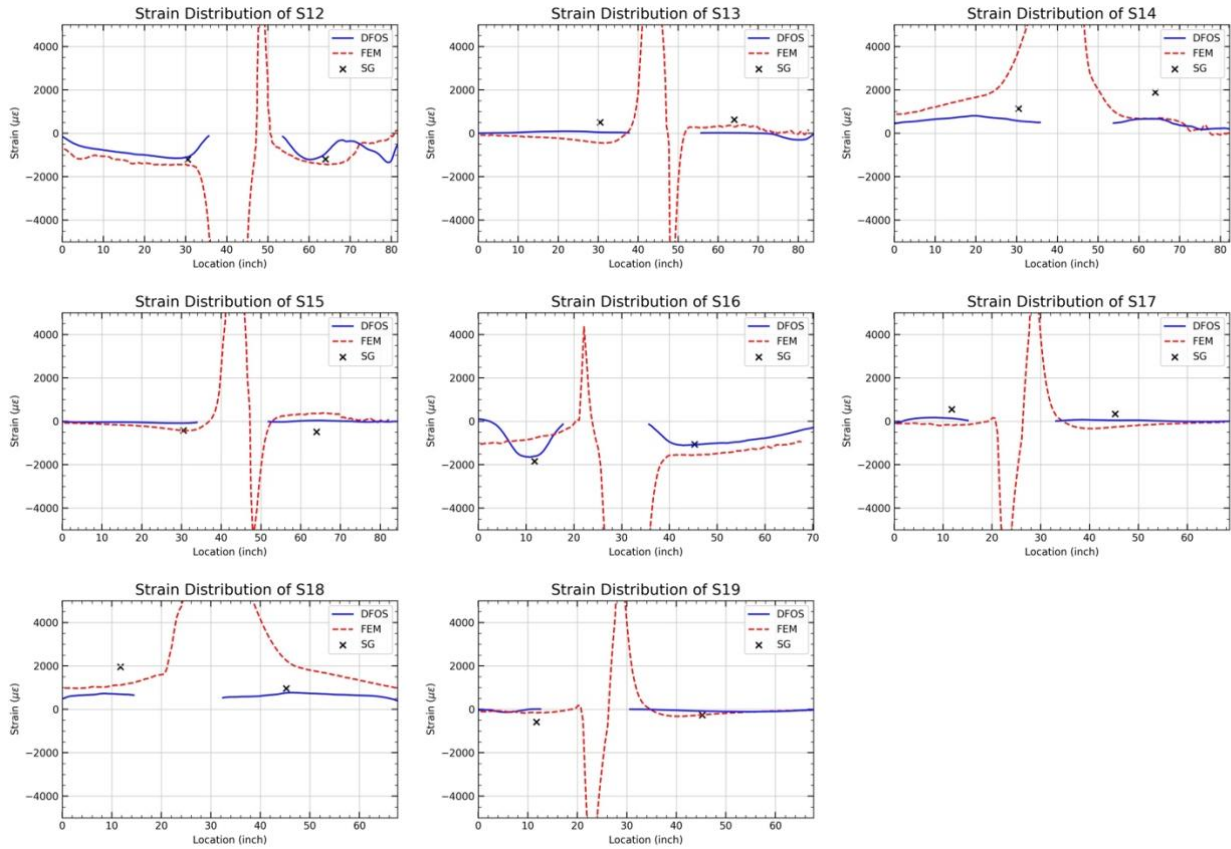
Test 1

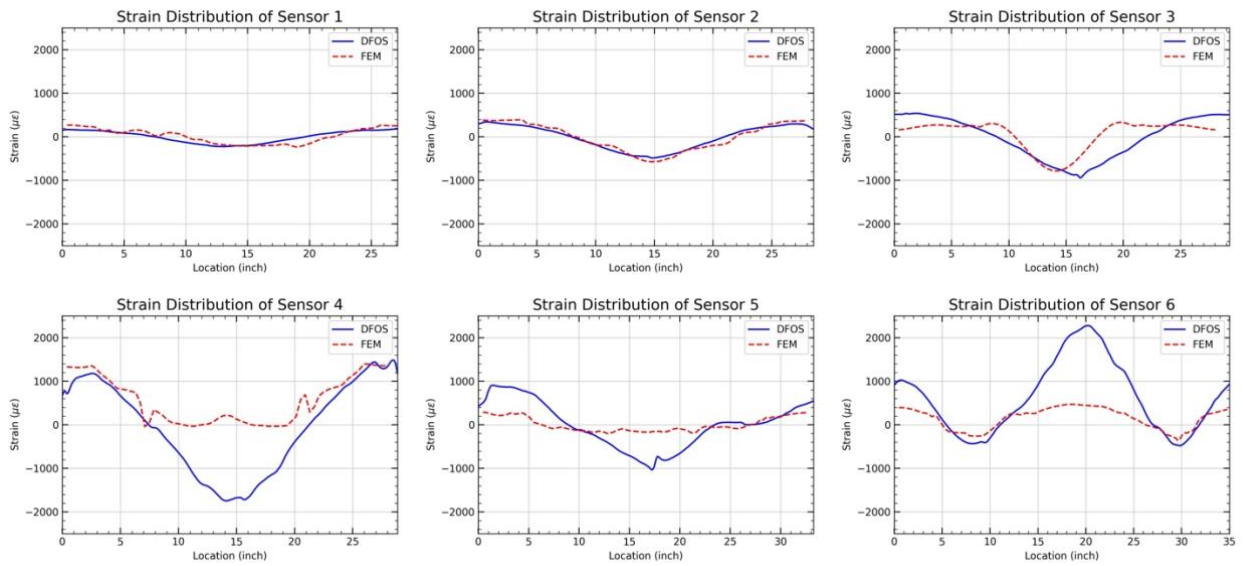**Figure C-1 Circumferential strain comparison**

Figure C-2 Longitudinal strain comparison
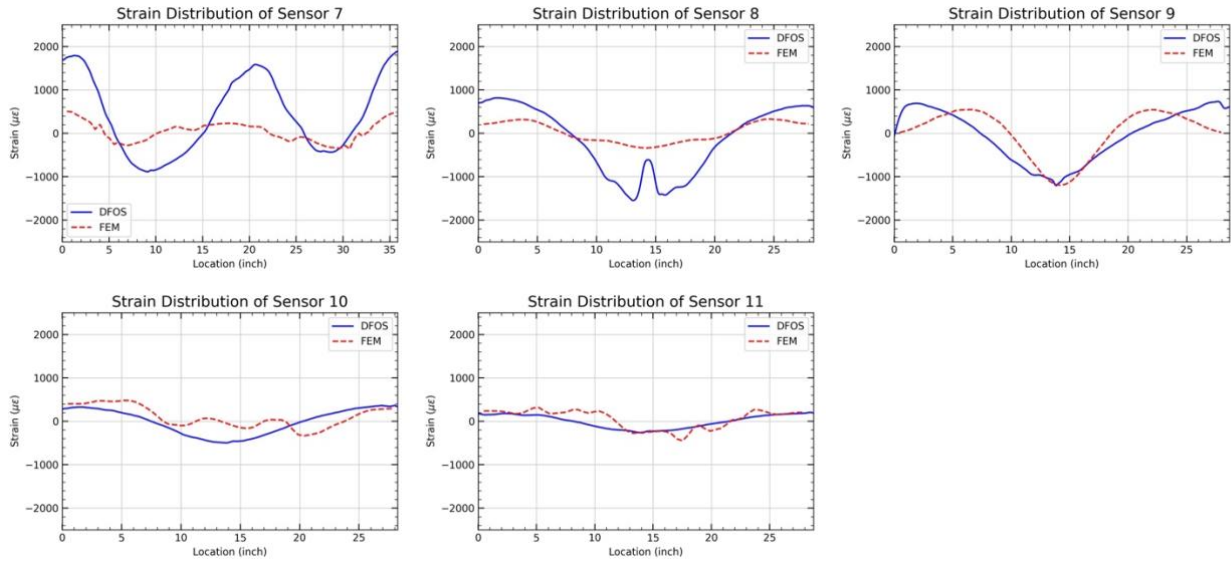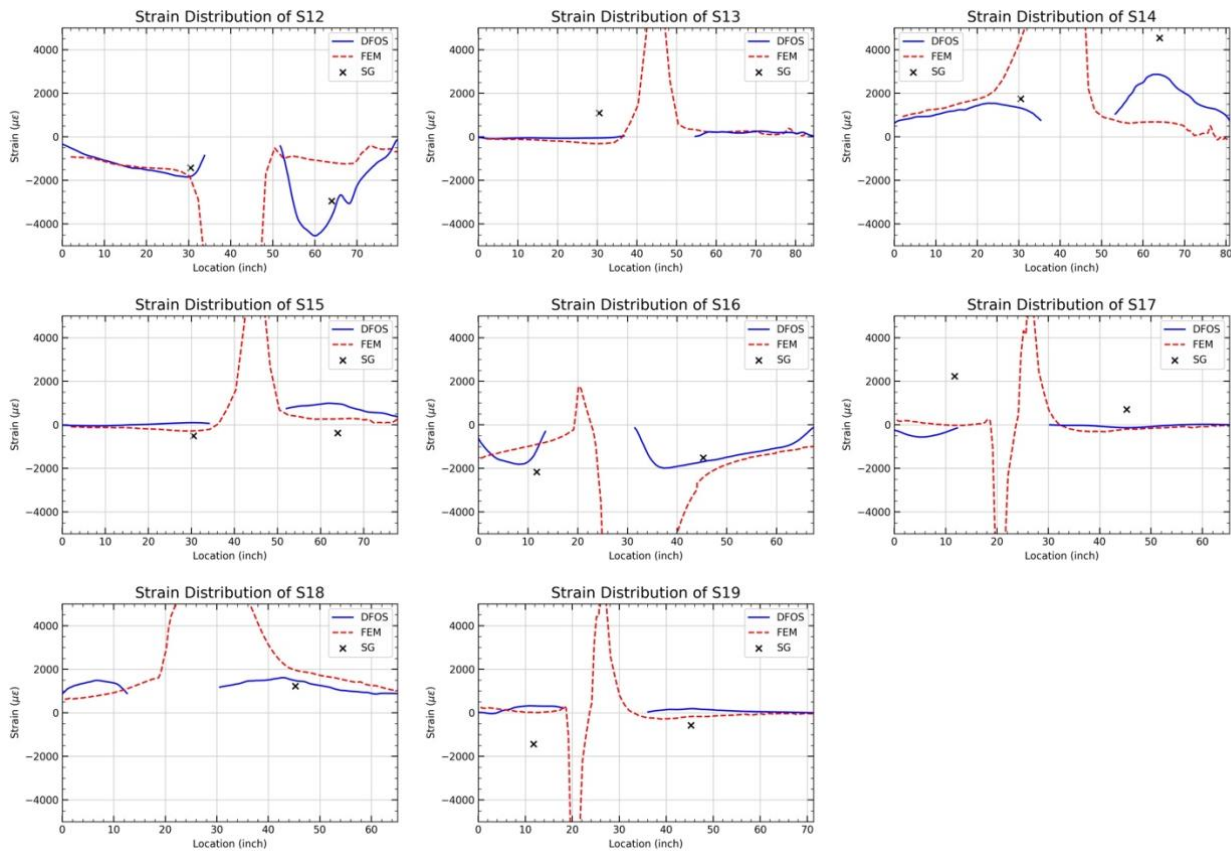
Test 2

Figure C-3 Circumferential strain comparison

Figure C-4 Longitudinal strain comparison